Tactile Sensors for Palm-Size Crawling Robots

Jaakko Karras
Ronald S. Fearing, Ed.
Ruzena Bajcsy, Ed.

Electrical Engineering and Computer Sciences
University of California at Berkeley

Technical Report No. UCB/EECS-2014-40
http://www.eecs.berkeley.edu/Pubs/TechRpts/2014/EECS-2014-40.html

May 1, 2014

Report Documentation Page	*Form Approved* *OMB No. 0704-0188*

1. REPORT DATE **01 MAY 2014**	2. REPORT TYPE	3. DATES COVERED **00-00-2014 to 00-00-2014**

4. TITLE AND SUBTITLE **Tactile Sensors for Palm-Size Crawling Robots**	5a. CONTRACT NUMBER
	5b. GRANT NUMBER
	5c. PROGRAM ELEMENT NUMBER
6. AUTHOR(S)	5d. PROJECT NUMBER
	5e. TASK NUMBER
	5f. WORK UNIT NUMBER
7. PERFORMING ORGANIZATION NAME(S) AND ADDRESS(ES) **University of California at Berkeley,Electrical Engineering and Computer Sciences,Berkeley,CA,94720**	8. PERFORMING ORGANIZATION REPORT NUMBER
9. SPONSORING/MONITORING AGENCY NAME(S) AND ADDRESS(ES)	10. SPONSOR/MONITOR’S ACRONYM(S)
	11. SPONSOR/MONITOR’S REPORT NUMBER(S)

12. DISTRIBUTION/AVAILABILITY STATEMENT

Approved for public release; distribution unlimited

13. SUPPLEMENTARY NOTES

14. ABSTRACT

15. SUBJECT TERMS

16. SECURITY CLASSIFICATION OF:			17. LIMITATION OF ABSTRACT	18. NUMBER OF PAGES	19a. NAME OF RESPONSIBLE PERSON
a. REPORT **unclassified**	b. ABSTRACT **unclassified**	c. THIS PAGE **unclassified**	**Same as Report (SAR)**	**63**	

Standard Form 298 (Rev. 8-98)
Prescribed by ANSI Std Z39-18

Acknowledgement

This report contains material that was previously published in:

J.T. Karras, D.W. Haldane, and R.S. Fearing, "Rapid-Manufacturable Hair Sensor Array for Legged Millirobots," in IEEE/RSJ Int. Conf. on Intelligent Robots and Systems, Vilamoura, Portugal Oct. 2012.

Material from the above publication is copyright 2012 IEEE, and is re-used here with permission.

Contents

List of Figures

List of Tables

Chapter 1

Introduction

Legged millirobots, like the biological organisms that they mimic, can readily adapt to a variety of complex environments. These robots can operate in rough terrain, confined spaces, and in the presence of obstacles such as foliage. This versatility makes legged millirobots an ideal solution to tasks requiring high maneuverability in difficult and uncertain environments. Examples might include searching through wreckage in the aftermath of natural disasters, or performing inspection and maintenance tasks within the interiors of buildings and other structures. Ideally, many of these tasks would be completed either autonomously or semi-autonomously, allowing human operators to focus on higher-level organization and control. In order to operate effectively without constant human guidance, legged millirobots must be equipped with adequate sensing capabilities to characterize and respond to their surroundings.

Vision and sonar systems could provide a piece of the needed functionality by detecting environmental features at a distance, and would likely play a role in any autonomous millirobot. A semi- or fully-autonomous millirobot would, however, also require reliable information regarding its immediate surroundings, particularly about surfaces that it contacts. To be effective, especially in dark, highly confined spaces, an autonomously-operating millirobot needs reliable contact sensing such as that provided by antennae or distributed tactile sensors.

Biology presents numerous solutions to the tactile sensing problem through the myriad of tactile sensing structures found in insects and mammals, such as touch-sensitive skin, hairs, whiskers, and antennae. In nature, such structures serve a wide range of sensory functions and much work has been done in recreating them for applications in mobile robotics. Wall-following behaviors have been implemented in both wheeled and legged mobile robots using artificial antennae and whiskers (Cowan et al. [3], Jung et al. [12], Lamperski et al. [13], Lee et al. [14]). Passive whiskers have been added to mobile robots to detect and recognize obstacles (Russell et al. [17, 18], Wijaya et al. [21]), and extensive work has been done in using whisker structures to identify textures and terrain (Fend et al. [4, 5], Fox et al. [6], Lepora et al. [15], Schultz et al. [19], Seth et al. [20]). All of these sensing structures share the commonality that they extend well beyond the body of the robot, detecting features that are a certain distance away. Important information can also be gained by sensing contact much closer to the body of the robot. For instance, short ground-facing whiskers were mounted around the feet of a quadrupedal robot to measure foot-ground interactions (Hirose et al. [8]).

This report presents work done in developing tactile structures for detecting and measuring body contact in rapid-manufactured millirobots such as DASH (Birkmeyer et al. [2]), DynaRoACH (Hoover et al. [10]), OctoRoACH (Pullin et al. [16]), and VelociRoACH (Haldane et al. [7]), and presents applications in which body sensing can be used to extract useful information from the environment. Two novel sensors are presented. The first, a binary hair-based sensor array, can be rapidly manufactured using a laminar process by virtue of its straightforward design. As an example application, the sensor was mounted to the bottom of a hexapedal millirobot and used to measure forward progress when running over simple obstacles. The second sensor discussed, an analog force-sensing bumper array, provides accurate contact force measurements using an inexpensive and lightweight design. This sensor was mounted to the front of a hexapedal millirobot and used to measure foot traction on unknown surfaces.

Chapter 2

Binary Hair Sensor Array

A low cost, rapid-manufacturable hair-based body contact sensor array was designed for use with lightweight, rapid-manufactured legged millirobots such as DASH, DynaRoACH, OctoRoACH, and VelociRoACH (Fig. 2.1). The sensor consists of a 5×4 (rows $\times$ columns) array of highly sensitive binary contact switches, where each switch is activated by a compliant polymer hair originating from the tip of the switch. These biomimetic hairs detect both shear and normal contact forces, enabling the sensor array to detect a wide range of body contacts. The compliance of the hairs also enables the sensor to conform to uneven surfaces, making it useful for robots operating in rough terrain. The hair sensor design is novel in that it can be fabricated using an entirely laminar roll-to-roll process that is compatible with the scaled Smart Composite Microstructures (SCM) fabrication methodology (Hoover et al. [9]) used to build the millirobots that it is designed for.

To demonstrate its usefulness, the hair sensor array was used to estimate the ground speed of a hexapedal millirobot as it traversed a simple obstacle. The sensor array was also used for the related sub-problem of detecting when the robot became high-centered, or caught on, an obstacle while trying to crawl over it. These tasks are highly relevant for small-scale robots operating in rough terrain where the results of locomotion are unpredictable, and robots need to be able to measure their forward progress. For both tasks, the hair sensor array was used to detect variation in ground contact along the bottom of the robot, and that variation then used to make inferences about the motion of the robot. These applications are presented in greater detail in section 2.5.

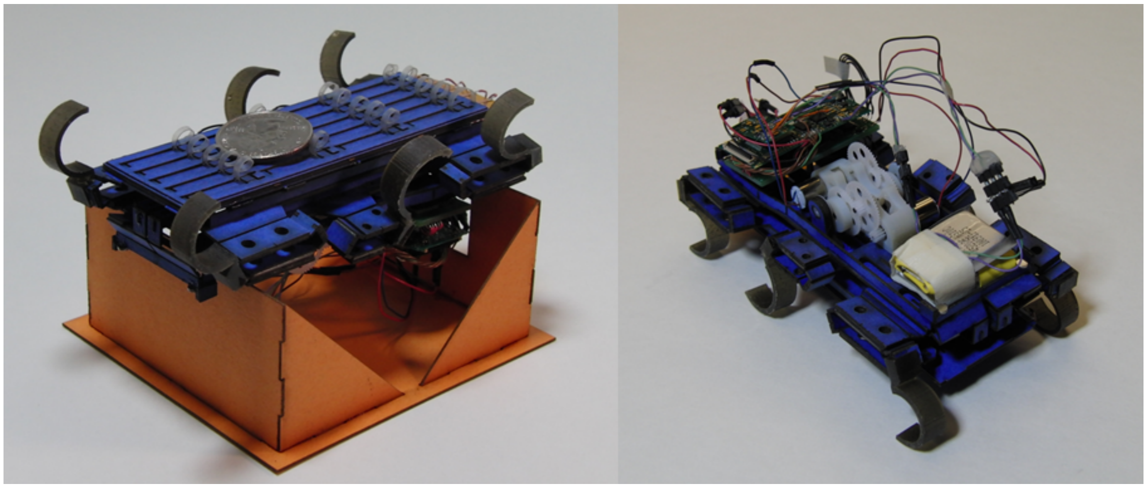

Figure 2.1: (Left) Hair-activated 5 × 4 contact sensor array mounted on bottom of a hexapedal millirobot. The array is 35 mm by 101 mm (width by length) and weighs 5 g. U.S. Quarter shown depressing second column of hairs. Robot is shown inverted on a supporting stand. (Right) Millirobot standing upright, with hair array mounted to bottom.

2.1 Design and Working Principle

The main objectives for the design of the hair sensor array were to achieve high sensitivity, to detect a wide range of body contacts, and to develop a sensor that can be produced using rapid roll-to-roll fabrication processes at low cost. These objectives are achieved using an array of switches, where each switch is activated by a curled, compliant hair mounted at the tip. Each switch activates a junction in a resistive row-column matrix, which is sampled element-wise by an embedded processor to determine the contact pattern on the sensor. The entire sensor is assembled from 13 thin layers of cardboard, copper, various polymers, and sheet adhesive through lamination and laser cutting. For the sensor array discussed in this report, the hairs have an average normal sensitivity of approximately 0.8 grams/hair, but the sensor design and fabrication methodology can be readily adapted to produce hairs of different sensitivities.

Mechanical Design

The hair sensor consists of an array of SCM switch structures, where each switch is activated by the loading of a compliant polymer hair at its tip (Fig. 2.2). The switches themselves consist of a lever arm (B) of rigid structural material hinged at one end through a polymer flexure (C). The sensor array discussed here uses four-ply cardboard (≈0.4 mm thick) as the structural material and 75 μm-thick PET film for the switch flexure hinges. Curled polymer hairs (A) are held in place at the tip of each switch lever by small blocks of cardboard that, together with adhesive, adhere the roots of the hairs to the lever tips. When the hairs are perturbed, either through normal or shear contact forces, the levers deflect downward, pivoting at their flexure hinges.

The hair-lever structures sit above two copper contact layers (D), separated by a small air gap. When deflected by the hairs, the switch levers bring the top copper layer into contact with a rounded solder contact positioned at the end of the bottom copper layer. The top copper contacts form the sensor array columns, and the lower copper contacts form the rows. While it did not present significant problems during this work, oxidation can be reduced by gold-plating the copper layers prior to assembly, although at added cost. Alternatively, the copper contacts could be replaced entirely with analog transducers, such as capacitive or optical units, for an analog sensor array.

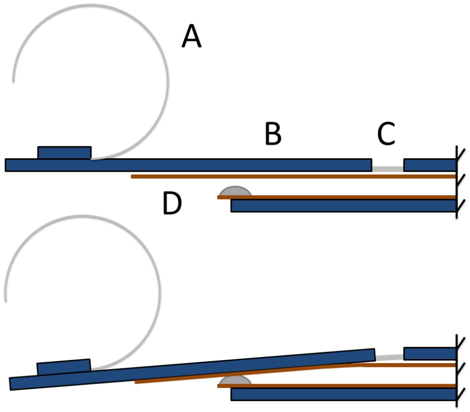

Figure 2.2: Hair-based switch shown in both the open (top) and closed (bottom) configurations. Structure consists of a curled polymer hair (A), a rigid lever arm (B), a polymer flexure (C) and copper contacts (D).

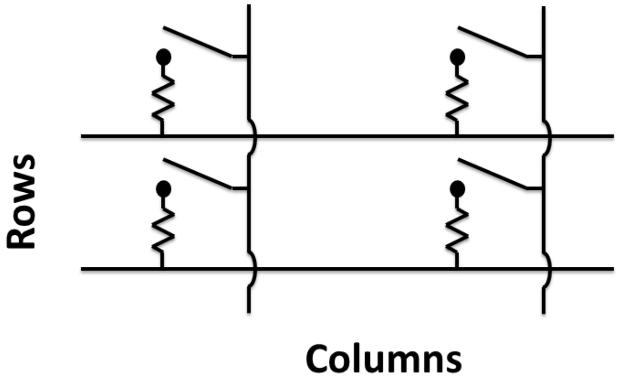

Figure 2.3: Schematic illustrating two rows and two columns of a resistive array of hair switches.

Electrical Design

The row and column conductors beneath each switch lever are part of a resistive array, with a resistor placed in series with each switch (Fig. 2.3). For the sensor used in this work, 10 kΩ resistors were soldered in series with each lower row contact. The resistors are needed to be able to localize the sources of contacts using the sampled electrical signals, since the absence of resistive elements at each junction would allow for cross-talk. Diodes could also be used, but resistors were chosen since these can ultimately be replaced with resistive ink to avoid discrete components, further improving manufacturability.

2.2 Rapid Laminar Fabrication

One of the key design features of the hair sensor array is that it can be fabricated using an entirely laminar process, in which the full sensor is assembled by stacking up layers of material via lamination, while forming the required mechanical features on the accumulating stack-up using a laser-cutter. Overall, the hair sensor array is the product of 13 separate layers that stack together to form the electrical contacts, switch levers and hairs (Fig. 2.4). This process is detailed in the following sections.

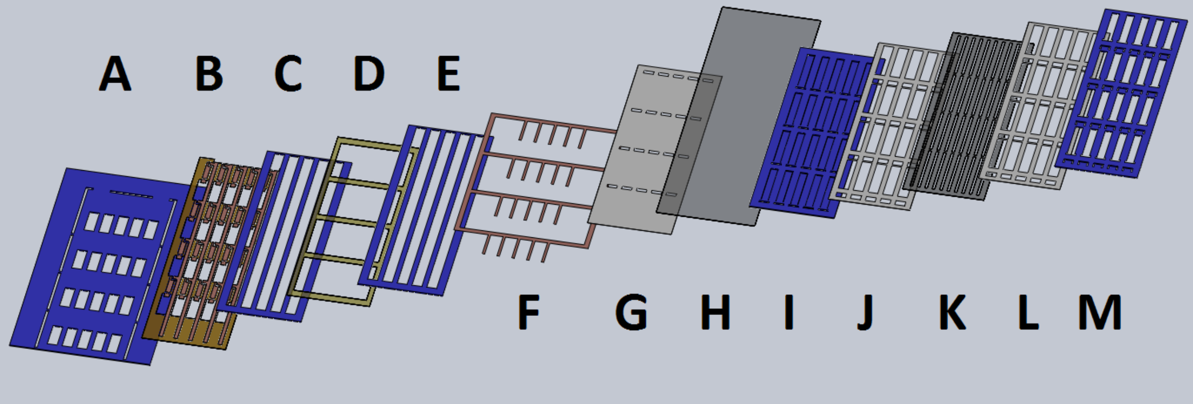

Figure 2.4: Layers that comprise the hair sensor array: (A) Base Layer (B) Bottom Contacts (C) Spacer (D) Insulating Polymer Film (E) Spacer (F) Top Contacts (G) Paper Backing (H) Flexure Polymer Film (I) Switch Levers (J) Pre-Cut Sheet Adhesive (K) Pre-Stressed Hair Film (L) Pre-Cut Sheet Adhesive (M) Hair Mounting Layer. For visualization purposes, layers I and M are shown with laser-cut features that are actually formed after lamination.

Lower Half of Sensor

Initially, the lower half of the sensor and the upper half with the hair-activated levers are built up independently, as two separate layered structures. The lower electrical contacts are formed by laminating a thin flex circuit (B) in between a rigid base layer (A) and a rigid spacer layer (C). The flex circuit contains the lower copper contacts and discrete resistors. An insulating polymer layer is then added (D), followed by another rigid spacer (E) to create a ≈1 mm gap between the flex circuit and the switch levers.

Upper Half of Sensor

The mechanical top half of the sensor begins with the formation of the hinge flexures (H & I). This follows a process similar to that described in (Hoover et al. [9]), with the exception that the flexure is only laminated to one rigid layer, not in between two, in order to keep the switch levers thin. A paper backing (G) is laminated to the underside of the levers to ensure that the electrical contact sides of the levers are uniform. The levers are then partially freed from the structure via laser-cutting. The levers are left partly connected at this point so that the hairs (L) can be attached with the levers still stationary.

Polymer Hairs

The curled hairs consist of a composite of 25 μm polypropylene (PP) film laminated together with 50 μm low-density polyethylene (LDPE) film. When laminated at a temperature of 177 °C (350 °F) and a pressure of 345 kPa (50 psi), the two films fuse together and the composite PP-LDPE film curls into a roll with a radius of curvature of ≈3-4 mm. This pre-curled hair film is then laid out flat, cut via laser to free the sides of the individual hairs, and embedded in a pre-stressed, flattened state between the levers and another structural layer (M). Selectively-cut sheet adhesive layers (J & L) hold the roots of the hairs between the two rigid structures.

Final Cuts

With the pre-stressed hair film in place, the upper and lower half-structures are laminated together with the upper electrical contacts (F) placed in between the two. The hair switches are completed by two sets of laser cuts: one to fully free the levers and a second to free the tops of the embedded hairs, which immediately curl out of the plane of the sensor due to their being in a pre-stressed state prior to the final cuts (Fig. 2.5). The full sensor is completed by simply freeing it from the supporting structure around the base (A), and by cutting away the sides of the column conductor layer (F) to electrically isolate the columns.

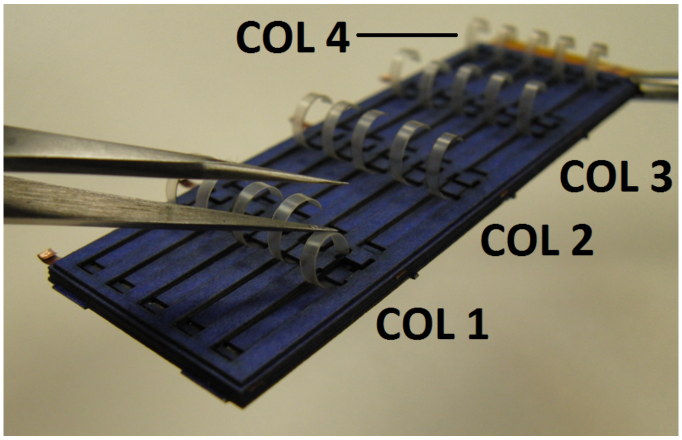

Figure 2.5: Completed 5 × 4 hair sensor array.

2.3 Read-Out Electronics

A 20 mm (W) by 43 mm (L) embedded electronics board was designed for collecting data from the hair sensor arrays (Fig. 2.6). The board, referred to as the SkinProc, uses an embedded 16-bit dsPIC33F microcontroller, a pair of analog multiplexers, and a two-stage amplifier circuit to multiplex and sample the binary switches in the hair sensor array. As configured for this work, the electronics scan the array at 2,000 samples per second for a frame rate of 100 Hz. Sampled data is communicated to the main robot-driver board, the ImageProc, over a UART serial connection. A schematic of the SkinProc, as configured for the binary hair sensor array, is provided in Appendix A.

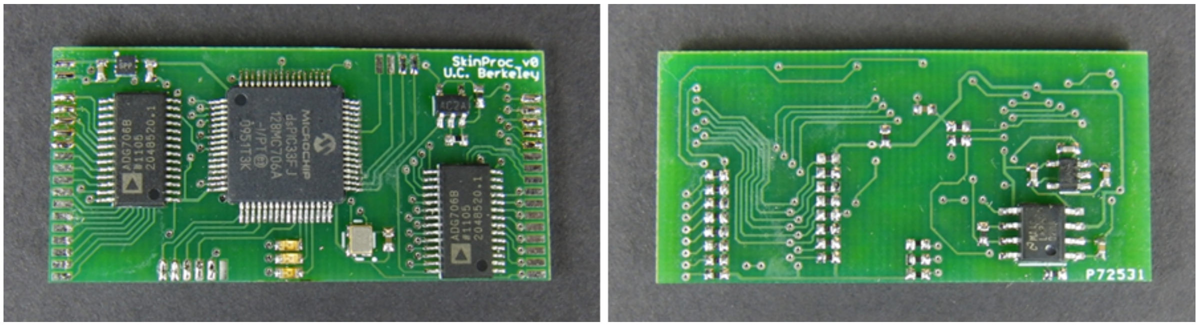

Figure 2.6: Images of front (left) and back (right) of SkinProc read-out electronics board. Board is 20 mm (W) by 43 mm (L).

2.4 Sensitivity

The average sensitivity of the hair-switches in the 5 × 4 array was computed by determining the minimum threshold weight at which different sized patches of hairs become active. Here, a patch of hairs was labeled as active if at least 2/3 of the loaded hairs were active. The results of these trials are plotted in Fig. 2.7. The dashed trend line is the least-squares fit (zero intercept) to the data points, indicating an average normal sensitivity of 0.79 grams/hair.

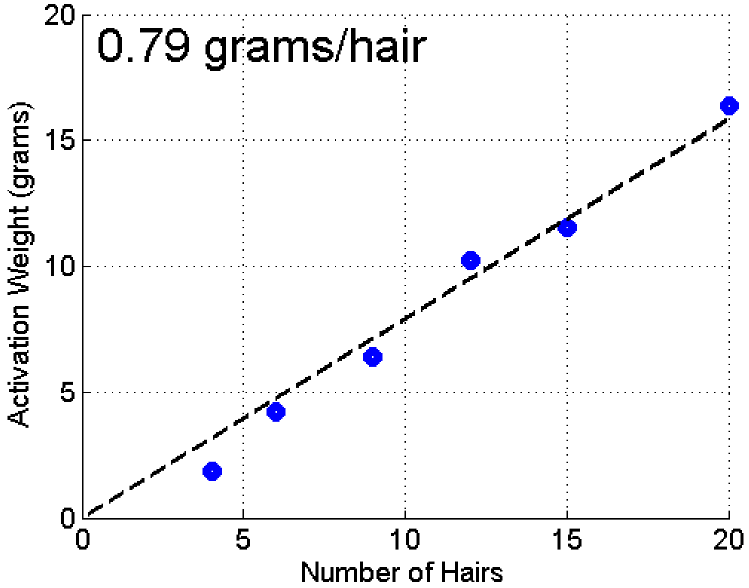

Figure 2.7: Total loading required for sensor activation as a function of the number of hairs loaded.

2.5 Application: Contact-Based Ground Speed Estimation

In order to test the hair sensor technology, the 5 × 4 hair array was mounted to the bottom of a hexapedal millirobot and a pair of contact-sensing algorithms used to detect high-centering and to estimate average ground speed when running over an obstacle. Both tasks are important problems when operating in rough terrain, where the high risk of entrapment requires that autonomous robots be able to reliably estimate their rates of forward progress and use that information to update their locomotive strategies when necessary.

Experimental Robot

A new hexapedal millirobot (Fig. 2.1), designed by Duncan Haldane, was used to study the performance of the sensor on a dynamic platform. The locomotion system of the robot comprises the chassis, transmission and legs. The SCM Process (Hoover et al. [9]) was used to fabricated a lightweight chassis and transmission that were rapidly optimized for compatibility with the sensor using an iterative design process. Unlike previous millirobots such as DASH (Birkmeyer et al. [2]) or DynaRoACH (Hoover et al. [10]), this robot features a new chassis with a static bottom plate to facilitate integration for the tactile sensor. The design maintains the proven feed-forward, alternating tripod gait kinematics of the DynaRoACH platform, but makes several modifications. The nominal touchdown and liftoff angles of ±42° were kept and the duty cycle remained at 0.5. However, the transmission was split down the sagittal plane, using one motor per side to drive two independent sets of three legs each. This split transmission enables robust steering control (Pullin et al. [16]). Dynamic simulations predict that running on curved legs expands the region of stable running (Jun et al. [11]), a conclusion substantiated by the performance of the highly dynamic modern RHex family of robots, which utilize semi-circular C-shaped legs. Semicircular legs for the robot were cast from a polyurethane elastomer (PMC-790 Smooth-On, Inc.). Parameters for the legs and the complete locomotion platform can be found in Table 2.1.

A 5 × 4 (rows by columns) hair sensor array was integrated with the experimental hexapedal millirobot. The sensor array was mounted against the bottom of the robot, hairs facing downward, with the rows oriented lengthwise along the robot, and the columns perpendicular to the direction of forward motion (Fig. 2.1).

Table 2.1: Physical Robot Parameters

Body Size	100 mm (L) 58 mm (W) 45 mm (H)
Total Mass	46.7 g (38.3 g without battery)
Leg Stiffness	$80\frac{N}{m}$
Leg Diameter	2.25 cm
Motors	2 x Didel MK07-3.3Ω
Gear Ratio	23.1:1

Experimental Setup and Methods

Ground speed estimation data was collected by running the robot over a rectangular box (25 mm W, 20 mm L, 7 mm H) attached rigidly to a textured tile surface (Fig. 2.8). The robot was set to run directly over the box at a variety of commanded speeds. The ground-facing sensor array was scanned at 100 Hz (100 full 5×4 frames per second), and the data logged to a Flash memory onboard the robot. Ground speed estimation was performed offline using the contact data collected during the data runs. All runs were carried out under an OptiTrack[1] motion capture system in order to obtain ground-truth position data for later comparison.

High-centering data was collected by replacing the rectangular box with a wedge, inclined at 7 degrees (Fig. 2.9). The wedge was designed such that the robot would become high-centered when run directly onto it. Again, contact data was collected at 100 Hz and stored in the onboard Flash memory during each run, and ground-truth was recorded using the motion capture system.

---

[1] NaturalPoint, Inc. OptiTrack: http://www.naturalpoint.com/optitrack/

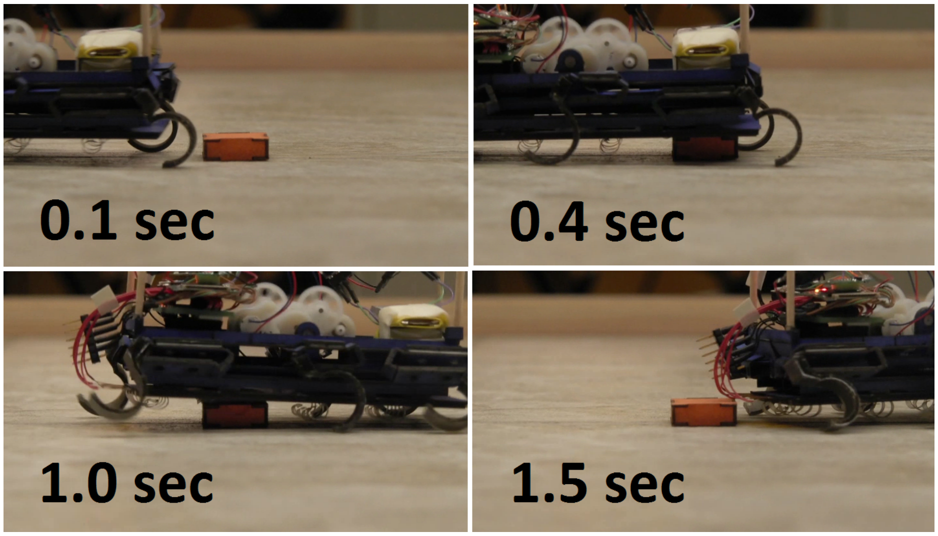

Figure 2.8: Frames from video footage of hexapedal millirobot running over experimental block obstacle.

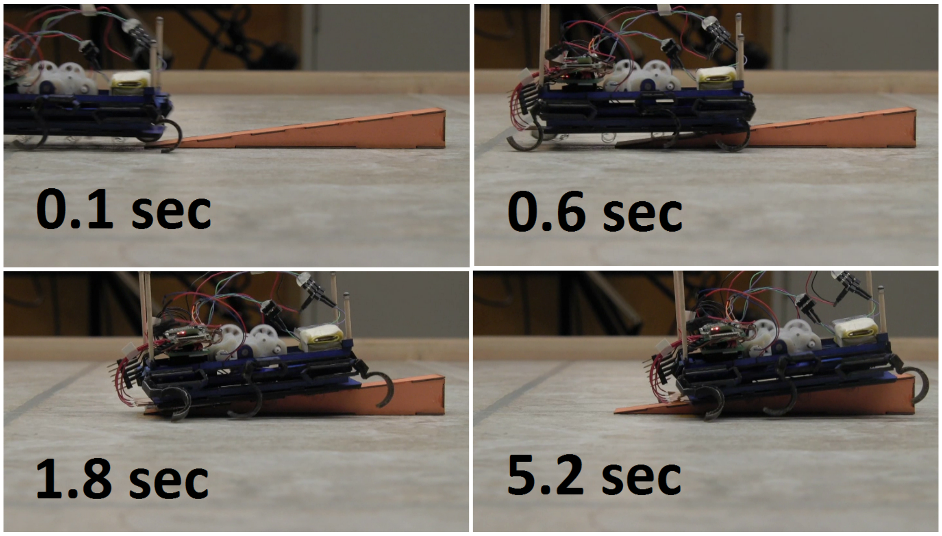

Figure 2.9: Frames from video footage of hexapedal millirobot running onto high-centering wedge.

Estimation Algorithm

Both the high-centering detection and ground speed estimation tasks are carried out by monitoring the average activation profiles for the four sensor columns over time. As the millirobot runs over an obstacle, one would expect the obstacle to register on each of the four columns, beginning with the leading column, followed by the second and so forth. For a single obstacle, each of the column activation profiles should contain a single pulse, lasting the duration that the obstacle was beneath the column. Because of the spatial separation between successive columns, there will be a time offset between the rising edge of the activation on one column and the same rising edge on the subsequent column. Knowing the spacing between columns, it is possible to estimate the average speed of the robot by matching edges (both rising and falling) across the sensor columns and recording the time delay between them (Fig. 2.10).

High-centering is detected by using the same column activation profiles and computing the pairwise maximum cross-correlation between the activation profiles of adjacent columns. In a forward-moving robot, the activation patterns of adjacent columns should show a high maximum cross-correlation value. This is because the peak cross-correlation value corresponds to the highest attainable degree of alignment between the two waveforms. As the robot becomes high-centered on an obstacle, however, the activation pattern corresponding to that obstacle will cease to propagate along the sensor array, resulting in poorly correlated activation profiles along the sensor. Thus, high-centering can be inferred when any of the pairwise correlations between adjacent columns drops beneath a minimum threshold.

Fig. 2.11 presents a block diagram of the contact-propagation algorithm. Sampled values from each of the four columns are passed through a low-pass filter (LPF block), after which they are averaged (μ block) to obtain a filtered mean activation for each column. These mean activation values are then passed into an edge detector, which applies thresholds to detect rising and falling edges. In the event that an edge is detected, it is stored in a queue of edges that can be referenced when edges are detected on the subsequent column. When matching edges are detected, the time delay between them is used to produce an estimate of the average ground speed. The activation waveforms encoded by the column edges are also correlated with one another in a pairwise fashion over a time window determined by the commanded speed, and the maximum value of each pairwise correlation is reported. If the maximum value of any pairwise correlation drops below a set threshold, the robot is inferred to be high-centered.

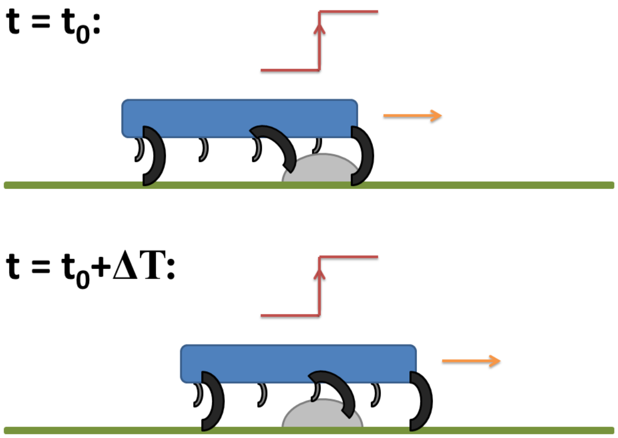

Figure 2.10: An obstacle propagating down the length of a running hexapedal millirobot. A rising edge is first detected on the leading column (top) and a matching edge is detected on the next column a time ΔT later (bottom).

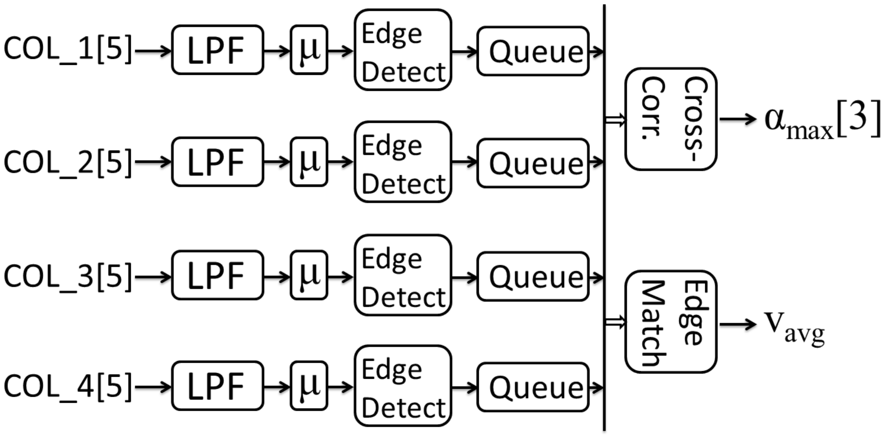

Figure 2.11: A high-level block diagram of the algorithms used to detect high-centering and to estimate average ground speed.

Results and Discussion

The results of a representative ground-speed estimation trial are plotted in Fig. 2.12. We observe from the column waveforms that the 7 mm tall obstacle produces a clear series of pulses along the columns of the sensor array as the robot crawls over it. As plotted, the first column (COL1) is the leading column at the front of the array. Because the obstacle propagates through all four columns, producing similar activation patterns for each column, the pairwise maximum correlation values between adjacent columns remain above the high-center detection threshold (0.05/1.0), and high-centering is not a concern. The edge-matching algorithm detects each of the six matched edges (three rising, three falling), and estimates the average ground speed of the robot during the intervals between the matched edges. For the most part, the estimated average ground speeds follow the ground-truth speeds.

Fig. 2.13 plots a collection of average ground speed estimates from a number speed estimation trials against their corresponding true average ground speeds, as determined from the motion capture data. The majority of the data points are clustered closely around the dashed y = x line, indicating that the hair sensor array can reliably estimate the average ground speed from the 7 mm tall box when running over it at speeds up to about 10 cm/s. The data does reveal a few erroneous estimates, most of which are overestimates. In context of this experiment, the likeliest cause of these overestimates is that a column initially missed the edge of the obstacle, possibly due to the robot bouncing, resulting in the rising edge for the obstacle being detected late.

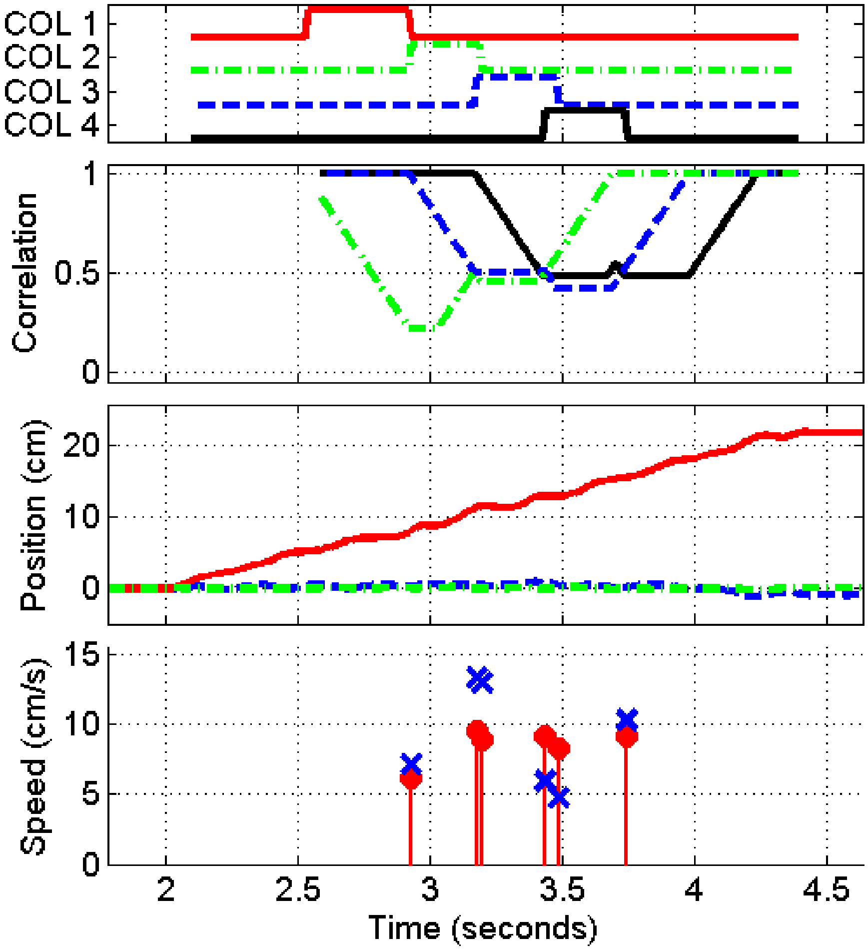

Figure 2.12: A representative ground speed estimation trial. Column activation waveforms are plotted (top), followed by pairwise maximum correlations for adjacent columns. The correlation line styles match the waveforms that they correspond to. Column waveforms are always correlated with those from their leading neighbor. The first column is not correlated. Correlation plots are followed by ground-truth position curves. Lastly, average ground speed estimates (red circles) are plotted against true values (blue Xs) computed from the ground-truth data. All plots are time-synchronized.

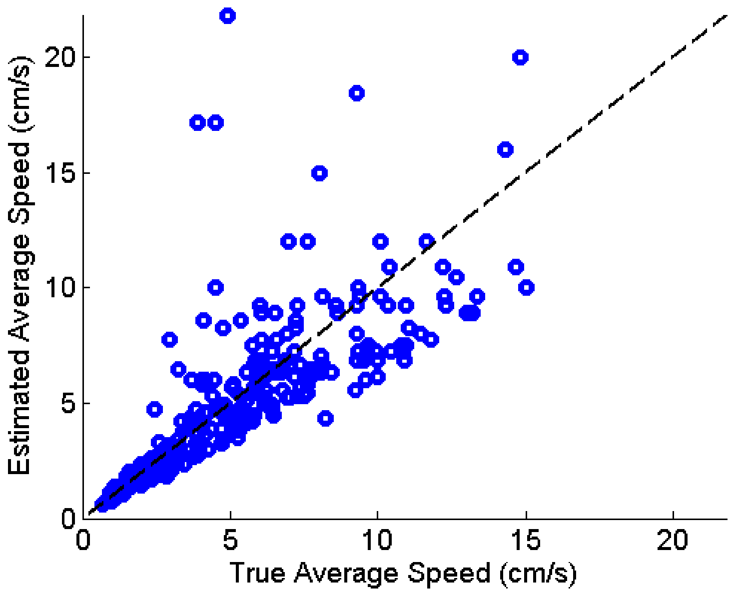

Figure 2.13: A collection of average ground speed estimates plotted against their corresponding true average speeds. Plot contains 248 data points accumulated from 42 data runs. Dashed line represents y = x.

An example high-centering data set collected using the 7-degree wedge is shown in Fig. 2.14. As seen from the ground-truth position data, the forward progress of the robot levels off as it pushes its way onto the wedge. As this occurs, the first two columns of the sensor array transition into a permanently-on state, while the rear two columns begin to toggle as the rear legs, which retain ground contact, pitch the rear of the robot up and down. The edge propagation algorithm detects the dissimilarity between the columns, and infers that the robot has become high-centered once the maximum correlation between the second and third columns drops below the 0.05 minimum correlation threshold (red circle).

The correlation-based algorithm consistently detected high-centering when the robot was run onto the wedge with commanded speeds in the mid- to high range of speeds tested, an approximate distribution of which can be seen in Fig. 2.13. At these speeds, the algorithm detected high-centering in 93% of the wedge trials (15 trials). For comparison, the same algorithm produced false positives on 22% of the non-wedge trials conducted at the same speeds (18 trials).

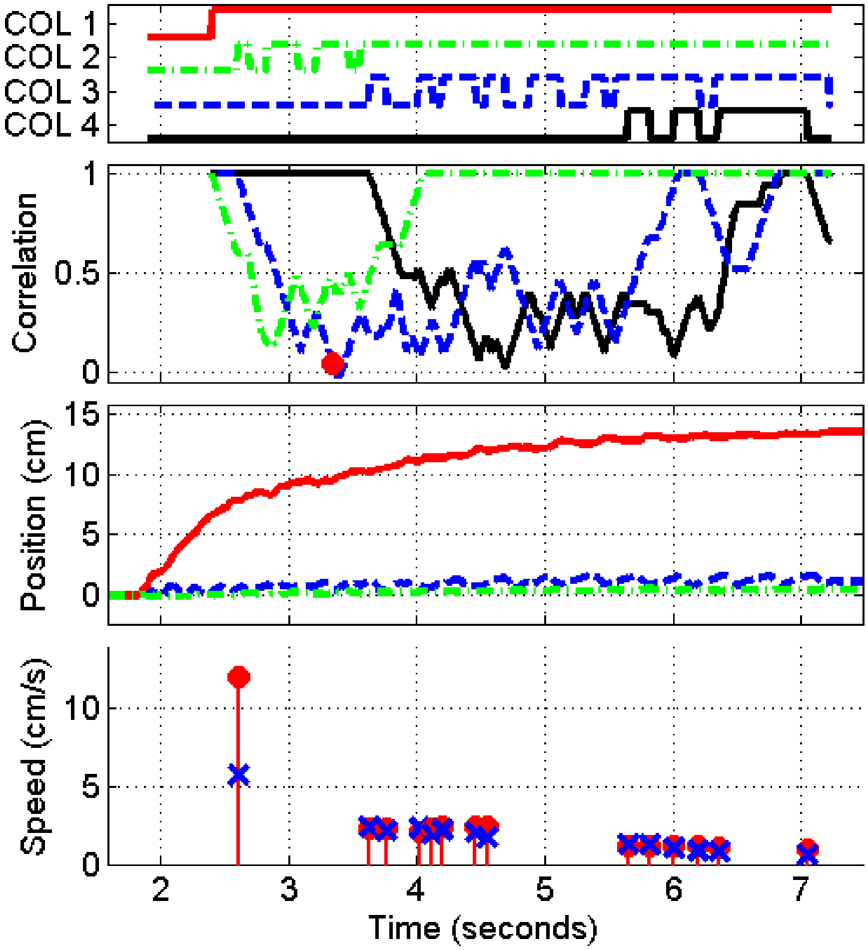

Figure 2.14: A representative high-centering trial. The red circle in the correlation plot indicates the first point at which a maximum correlation value drops beneath a threshold of 0.05.

Chapter 3

Force-Sensing Bumper Array

The binary nature of the hair sensor array discussed in the previous chapter allowed for a straightforward design and convenient fabrication methodology, but limited the information that the sensor could provide. It was shown that such a sensor can provide useful data on a millirobot's motion over ground-based obstacles by monitoring the propagation of contact along the array, but more could be achieved with a sensor capable of resolving a range of both force and deformation. Specifically, the ability to measure contact forces, and not just the presence of contact, could provide a millirobot with information about the material properties of surfaces, forces encountered during motion, and so forth. Furthermore, being able to extract a continuous signal for sensor deformation, combined with the inherent periodicity of the millirobots' motion at steady-state, opens up the possibility of frequency-domain techniques not afforded by a binary sensor. To take advantage of these possibilities, an analog tactile sensor was developed using rapid-manufacturing techniques compatible with the fabrication of SCM millirobots.

The analog tactile sensor consists of an array of rapidly-manufactured force-sensing elements, arranged on a cylindrical bumper structure that attaches to the front of a legged millirobot (Fig. 3.1). The motivation behind incorporating the sensor into a front-mounted bumper is that this configuration allows the robot to acquire real-time force measurements when running into obstacles. This information can be used, for instance, to measure the traction that the robot's legs can provide in unknown terrains, and therefore how much pushing-force can be generated. This application will be presented later in section 3.4.

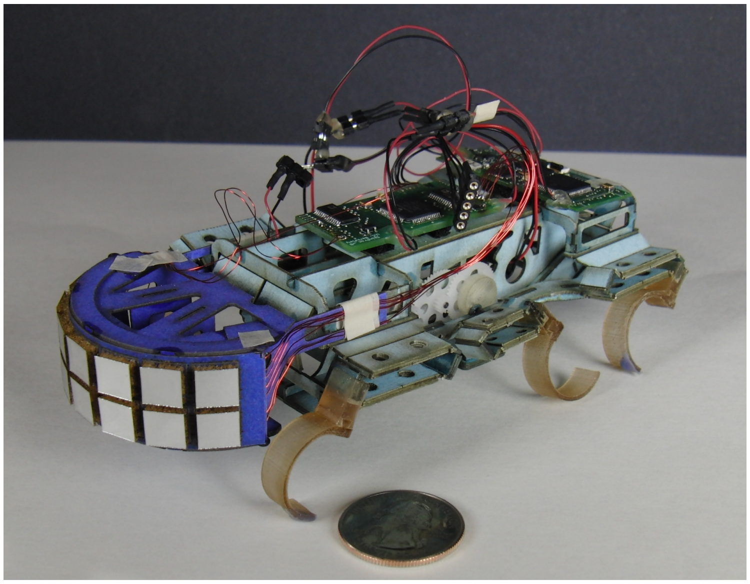

Figure 3.1: Front-mounted, analog tactile bumper array attached to hexapedal millirobot. U.S. quarter shown for size comparison.

3.1 Design and Working Principle

The force-sensing bumper consists of three main subcomponents: a laser-cut cardboard mounting structure, a 2 × 7 array of proximity sensors mounted to a flex-circuit, and an outward-facing 2 × 7 array of foam-based sensory structures (Fig. 3.2). The bumper array measures contact force by measuring the deformation of the foam sensory structures, which compress under load. Deformation is quantified by the array of proximity sensors which measure the distance to the reflective surfaces of the foam structures. Each proximity sensor produces an analog voltage level that varies with distance to the reflective surface. These voltage levels are sampled and digitized by a modified variant of the SkinProc embedded board used previously with the binary hair sensor array.

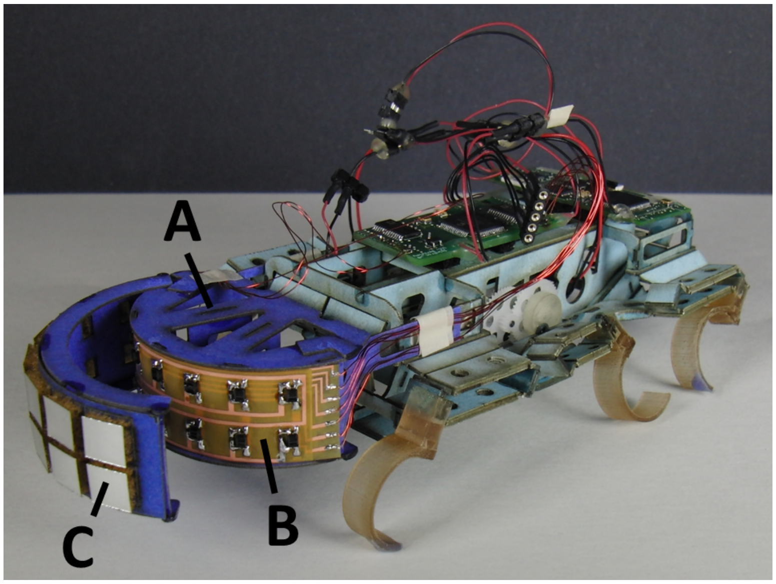

Figure 3.2: Image showing the three subcomponents of the force-sensing bumper: cardboard mounting structure (A), array of proximity sensors on flex-circuit (B), and outer layer of foam-based sensory structures (C).

Mechanical Design

Mechanically, the tactile bumper consists of a 2 × 7 array of mechanically isolated force-sensing taxels attached to the front of the hexapedal millirobot through a cardboard mounting structure. The mounting structure positions the taxels sufficiently far from the body of the robot that they clear the front legs. The front of the structure forms a cylindrical surface, which is both simple to fabricate and facilitates pushing through deformable obstacles. Each taxel consists of a reflective Mylar-film patch supported on foam walls above a Sharp GP2S60 proximity sensor. A cross-section illustration of a single taxel is provided in Figure 3.3.

The force-sensing taxels are designed to exhibit two sensitivities, meaning that they have greater sensitivity at small deformation, to detect smaller contact forces, and then become less sensitive at larger deformation, to increase the saturation force. The purpose for this bi-sensitivity is to increase the range of forces that can be detected, by allowing the robot to detect small forces in the high-sensitivity deformation range, and much larger forces in the low-sensitivity range. In terms of design, this is accomplished by having two sets of foam

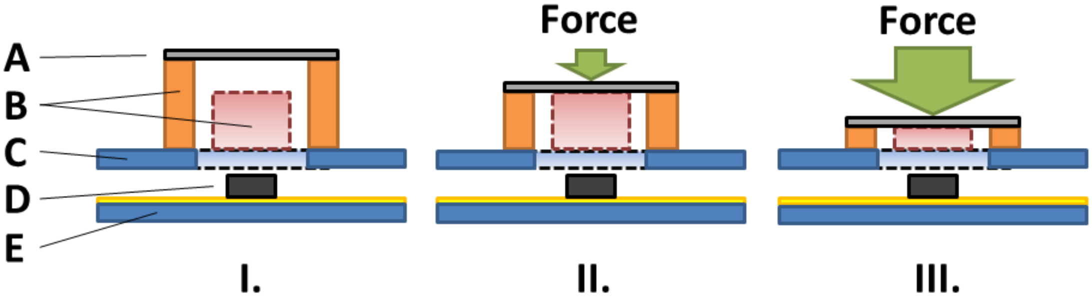

Figure 3.3: Cross-section illustration of force-sensing bumper taxel. Taxel structure consists of 2 mil thick reflective Mylar film (A), Outer and inner urethane foam walls (B), Foam-supporting cardboard layer (C), Sharp GP2S60 proximity sensor on flex circuit (D), and Bumper mounting structure (E). The taxels exhibit bi-sensitivity, with small forces deforming only the outer foam walls (I to II) and larger forces deforming both the outer and inner foam walls (II to III).

walls beneath the reflective Mylar-film patches, with one set of walls being taller than the other (Fig. 3.3). For small contact forces, only the taller, outer foam walls are compressed, allowing these forces to produce a measurable deformation. For larger contact forces, the reflective Mylar-film patches compress both the outer and inner foam walls, which stiffens the structure and allows larger forces to be measured before saturation.

Electrical Design

The 2 × 7 array of proximity sensors is configured as a crossbar-switch, allowing each sensor to be sampled individually. A schematic of the proximity sensor array is provided in Appendix C. Each of the Sharp GP2S60 units consists of an infrared emitter, paired with an infrared photodetector. To sample any given proximity sensor, the row containing the sensor is first driven to 3.3 V. Then, after a short delay, the current in the column corresponding to the sensor is converted to a voltage and sampled by an ADC. A schematic of the analog SkinProc variant used to sample the proximity sensors is given in Appendix B.

3.2 Fabrication

The tactile bumper mounting structure, proximity sensor array flex-circuit, and foam sensory structure array are each fabricated separately and then assembled together to complete the bumper. This fabrication process is described in the following sections.

Sensor Mounting Structure

The bumper mounting structure is assembled from laser-cut planar pieces. The uppermost piece in Figure 3.4 (left), which is curved during assembly to form a surface for mounting the flex-circuit, is cut from a single layer of 4-ply cardboard (approx. 0.3 mm thick). The remaining components require greater rigidity and are cut from two layers of the same cardboard, laminated together with sheet adhesive. The final assembled structure is shown in Figure 3.4 (right).

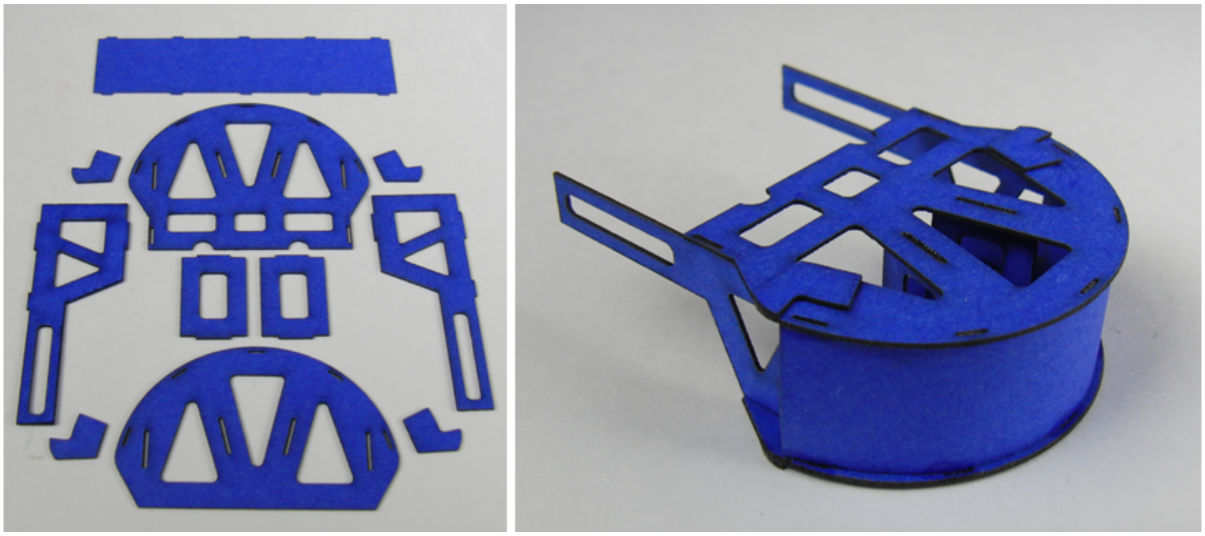

Figure 3.4: (Left) Laser-cut pieces used to assemble tactile bumper mounting structure. (Right) Completed tactile bumper mounting structure.

Flex-Circuit Array

The flex-circuit for the proximity sensor array is fabricated in-house from two layers of etched copper-clad Kapton (Dupont AC2500E). To begin, adhesive-lined 50μm Kapton film is applied over the copper, but without lamination. An etch mask is then patterned onto the Kapton film with a UV laser-cutter, using enough passes to cut through the Kapton film but not the underlying copper-Kapton laminate (Fig. 3.5 a). The unwanted copper regions are exposed by peeling away everything but the etch mask. The mask is then bonded to the copper via lamination (Fig. 3.5 b). The samples are etched in ferric chloride to remove unwanted copper (Fig. 3.5 c), and the mask removed by dissolving the adhesive holding it down with acetone (Fig. 3.5 d).

With the upper and lower layers fully etched, the flex-circuit is completed by simply laminating the two layers together with a layer of sheet adhesive in between (Fig. 3.6 top). The flex-circuit is then populated with Sharp GP2S60 proximity sensors and resistors. Traces on the two layers are also connected electrically with simple vias by creating solder bridges through windows cut into the upper layer. The completed sensor electronics layer are shown in Figure 3.6 (bottom). Magnet wire is soldered to the row and column traces of the circuit, and the circuit attached to the front of the bumper mounting structure (Fig. 3.7).

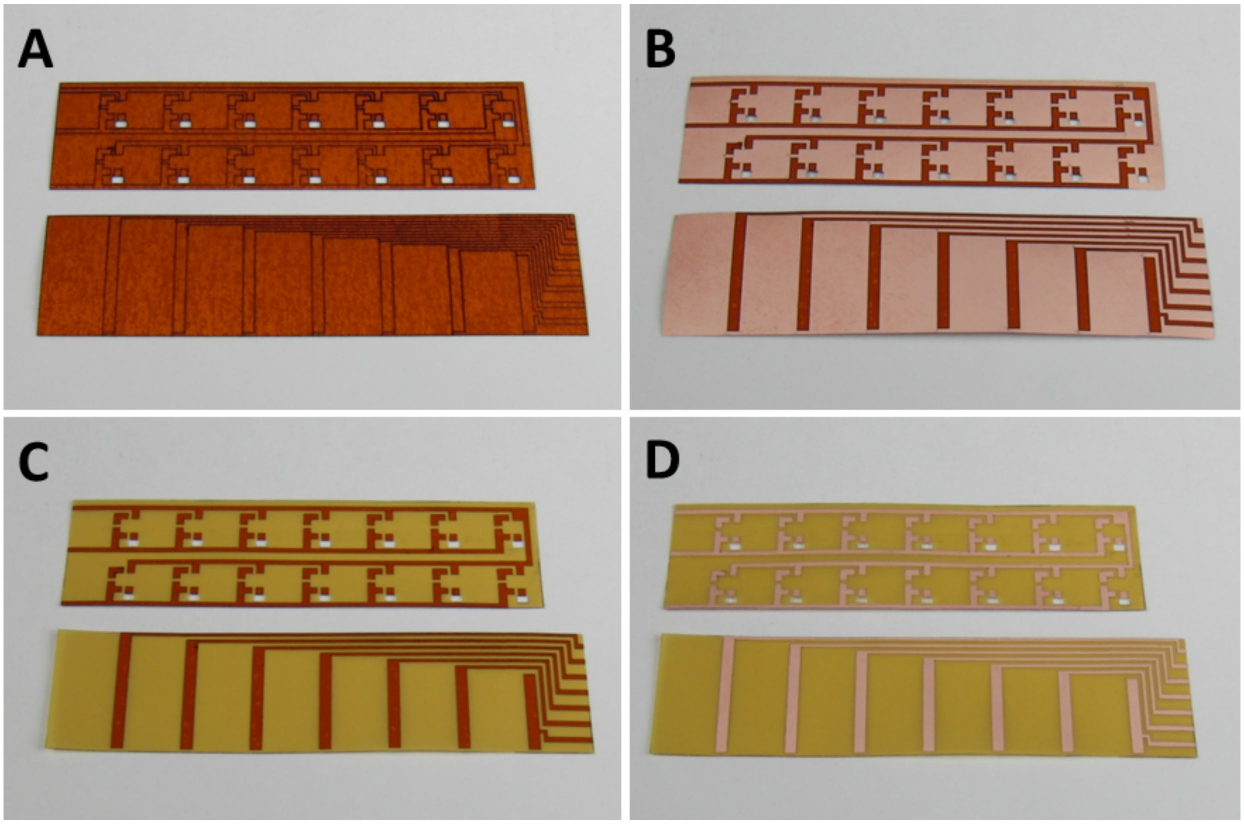

Figure 3.5: (A) Copper-coated Kapton with mask applied and patterned. (B) Unwanted mask removed to expose unwanted copper. (C) Unwanted copper etched away using Ferric Chloride. (D) Remaining mask removed, leaving top and bottom layers of flex circuit.

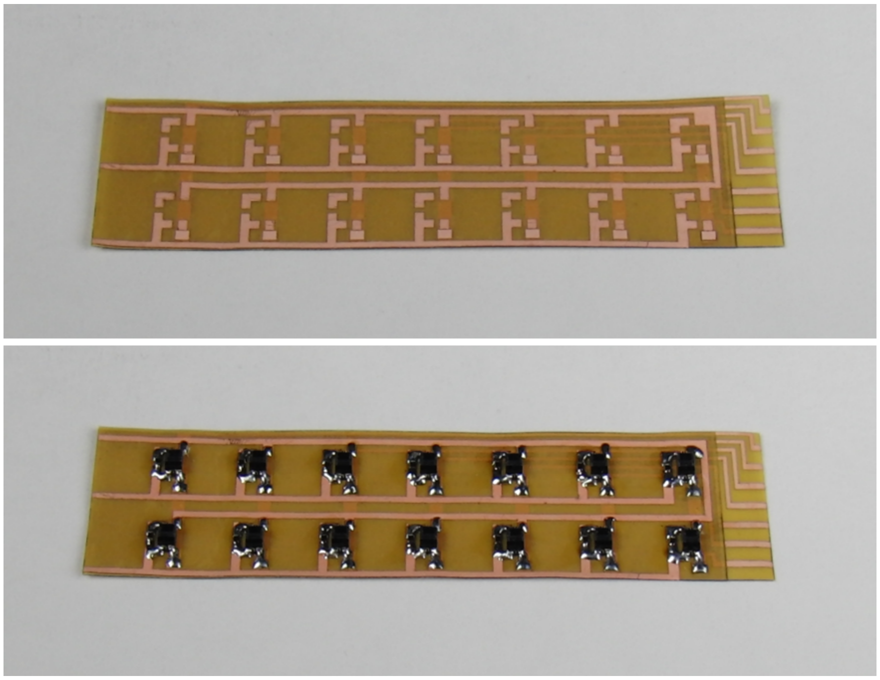

Figure 3.6: (Top) Completed bare flex circuit. (Bottom) Populated proximity sensor array.

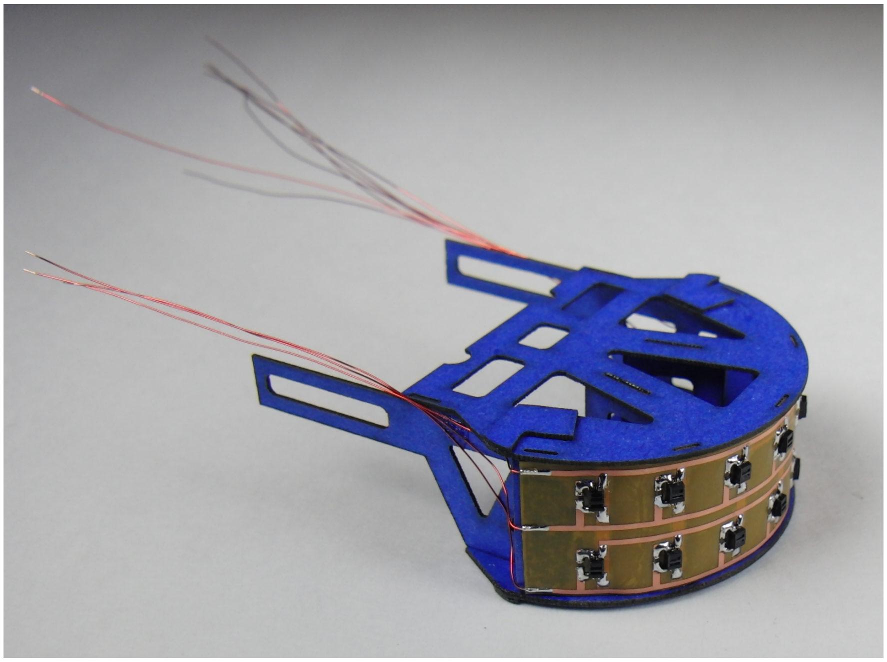

Figure 3.7: Proximity sensor array attached to front of tactile bumper mounting structure.

Foam Sensory Structure Array

The foam sensory structures that sit above the array of proximity sensors are formed through a laminar process involving the incremental build-up of features through lamination and laser cutting. The process begins with patterning a cardboard base layer. A patterned layer of sheet adhesive is laminated to the cardboard, and regions of the adhesive are then exposed by scoring, via laser, and removing portions of the paper backing (Fig. 3.8).

The exposed adhesive regions are used to anchor down the inner foam wall features. To do this, foam with a nominal thickness of 2.6 mm is laminated onto the adhesive (Fig. 3.9 top). In the fabrication sequence shown here, a sheet of 2.6 mm thick foam was not available, so foam strips of that thickness were laser-cut from thicker foam to provide the desired features. Ideally, however, the discrete strips would be replaced with a single sheet to streamline fabrication. With the foam laminated onto the cardboard base, the inner foam walls are formed by laser-cutting their outlines and removing the excess foam, which was not exposed to adhesive (Fig. 3.9 bottom).

To form the taller, outer walls of the foam sensory structures, an approximately 3.2 mm thick foam sheet is patterned via laser and laminated to a 2 mil thick reflective Mylar film. The combined foam-Mylar sandwich is then laminated onto the cardboard base, using the remaining sheet adhesive at the sides of the inner foam walls (Fig. 3.10). With the taller foam anchored down onto the cardboard base, the individual structures are isolated from one another by laser-cutting their outlines into the Mylar and foam and peeling away the excess material left in between. Lastly, the final outline for the cardboard base is cut around the array. The completed array, with the bi-sensitive foam structures, is shown in Figure 3.11.

In order to attach the foam structures to the remainder of the tactile bumper, the cardboard base anchoring the foam structures is curved onto two laser-cut mounting pieces that allow the foam structure array to be slid onto the front of the bumper mount (Fig 3.12, left). The total weight of the assembly shown in Figure 3.12 (right) is 3.7 grams.

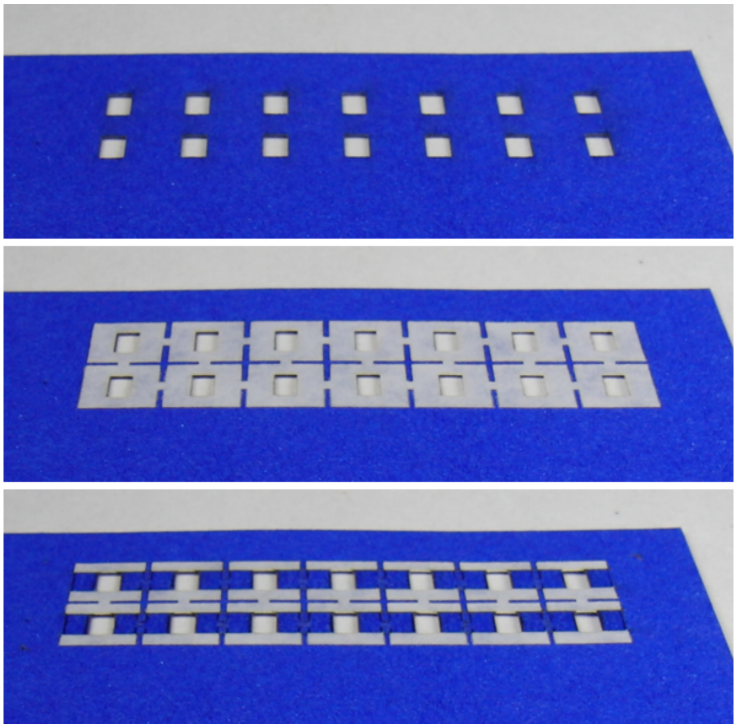

Figure 3.8: (Top) Patterned cardboard base for sensory foam structures. (Middle) Patterned sheet adhesive laminated over cardboard base. (Bottom) Regions of sheet adhesive exposed for anchoring inner foam walls.

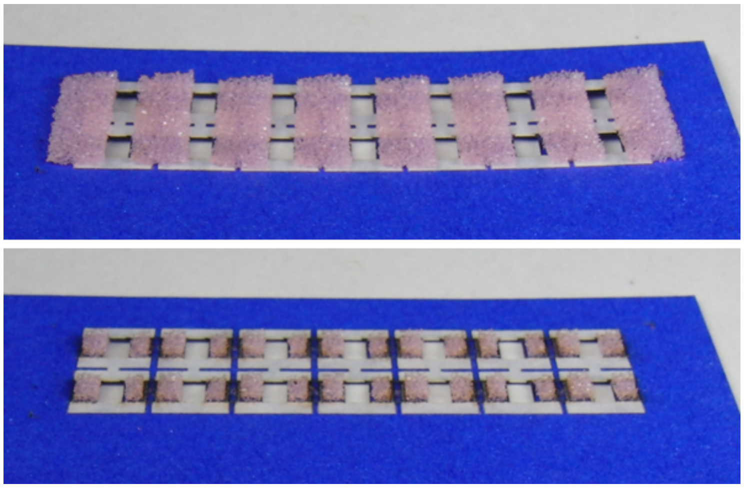

Figure 3.9: (Top) Foam strips laminated down onto exposed adhesive regions. (Bottom) Inner foam walls laser-cut from foam strips.

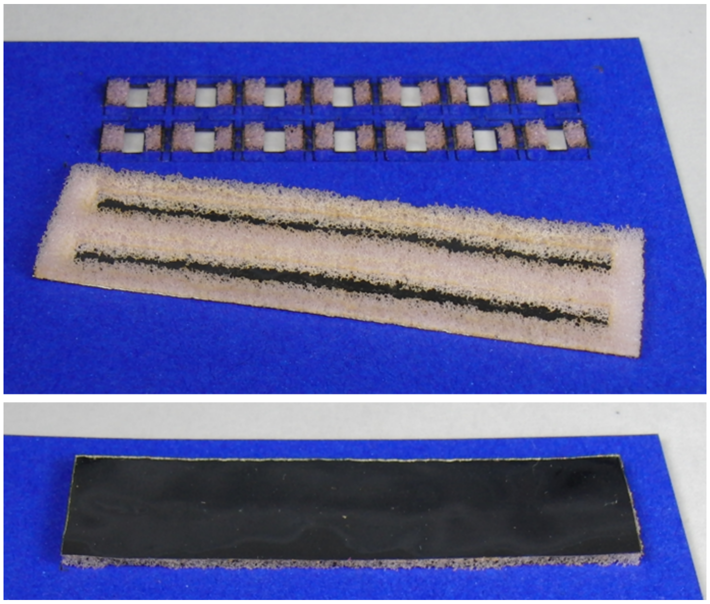

Figure 3.10: (Top) Taller, patterned foam is laminated onto reflective Mylar-film, to be placed onto adhesive exposed along sides of inner foam walls. (Bottom) Taller foam laminated onto cardboard base.

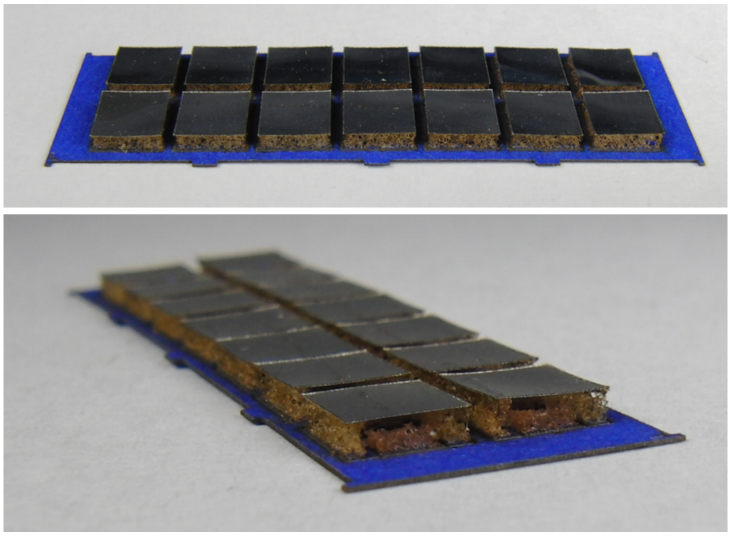

Figure 3.11: (Top) Isolated foam structures are isolated by cutting through Mylar-film and underlying foam, but not cardboard base. Excess material is peeled away from in between foam structures, and an outline is cut into the cardboard around the array. (Bottom) Bi-sensitive structure. Taller, outer foam walls support reflective Mylar-film patches over shorter, inner foam walls.

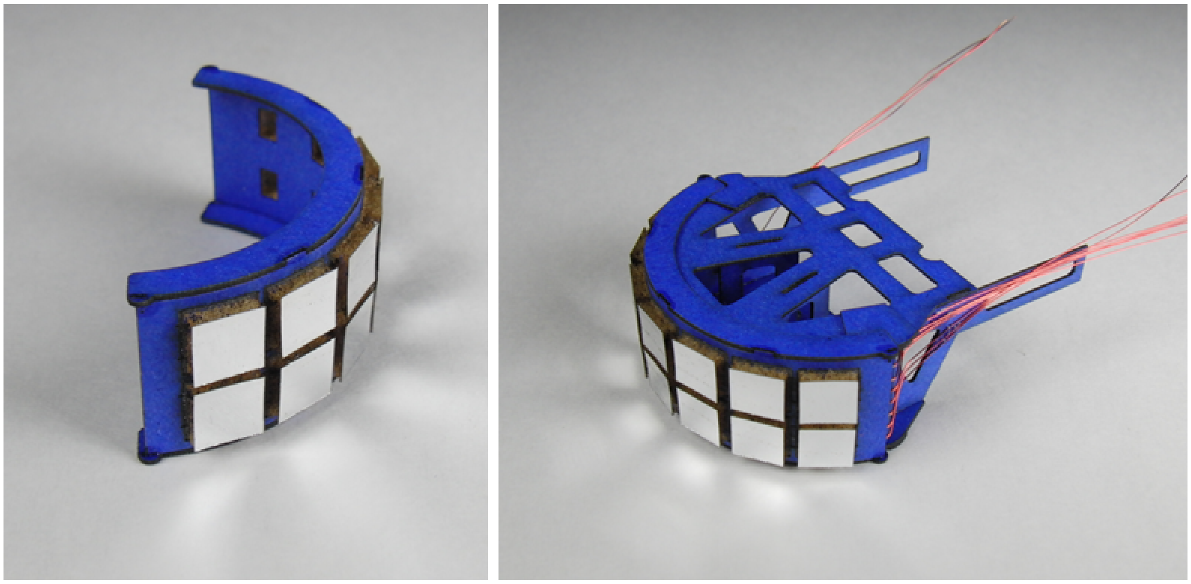

Figure 3.12: (Left) Completed foam structure array, attached to laser-cut mounting pieces. (Right) Foam structure array mounted to front of tactile bumper structure and over the electronics layer. Total weight is 3.7 grams.

3.3 Sensor Characterization

In order to characterize the temporal response and force sensitivity of the taxel array, step response data was collected for a single taxel for a range of loads. Positive step responses were collected by manually releasing a weighted slider onto the taxel. Three representative responses, each of increasing loading, are plotted in Figure 3.13. Negative step responses were collected by manually lifting the same weighted slider off of the taxel. Representative responses, again for increasing loading, are plotted in Figure 3.14. It should be noted that since the slider was both lowered onto and removed from the taxel by hand, the inputs used to produce these responses likely deviated slightly from pure step inputs.

The step responses show that the foam taxels have low temporal noise at steady state, both with and without the applied loads. The taxels also exhibit sufficiently quick response, with a sensor bandwidth on the order of 10 Hz, for use on a millirobot operating quasi-statically in rough terrain. Five trials were conducted for each of seven loading configurations. These trials reveal that the taxel produces consistent steady-state levels for the applied loads (see error bars in Figure 3.15), and returns to consistent levels after loading is removed.

The steady-state levels from each set of trials were averaged together and used to produce the force sensitivity plot in Figure 3.15. As can be seen from the plot, the taxel exhibits a non-linear response to applied force, with sensitivity leveling off towards the end of the range of forces tested. Over the first 25.2 gf, the taxel response increases 925 ADC counts, for an average resolution of 0.027 gf/lsb.

A plot of the taxel's sensitivity to displacement is given in Figure 3.16. The plot presents the responses of four individual taxels to being compressed with a micrometer. The taxel used for the force step response and force sensitivity data is plotted in black. As can be seen from the curves for the individual taxels, the responses are qualitatively similar, but are not identical and have slightly different offsets, likely due to slight deviations in their fabrication. These deviations can be accounted for by collecting calibration data for each individual taxel.

The force sensitivity data from Figure 3.15 was used to estimate the force that was required to achieve each of the displacements plotted in Figure 3.16. The resulting estimated force versus displacement curve is given in Figure 3.17. As can be seen from the plot, the pixel exhibits two clear stiffness intervals with lower stiffness up to about 1.2 mm of displacement and significantly higher stiffness for larger displacements. This confirms that the outer and inner foam wall structure achieves the desired stiffness profile.

An additional whole-bumper force calibration was performed by releasing a weighted slider with a rigid, flat plate against the front of the taxel array. The results of this calibration are plotted in Figure 3.18. Each data point represents the average total steady-state response of all the taxels in the array for the corresponding degree of loading. Each data point represents the mean of the steady-state from five positive step response trials. As can be seen from the plot, the whole-bumper sensitivity follows a trend similar to that of a single taxel but with a less pronounced change in sensitivity over the range of applied forces. The whole-bumper force calibration will be used in the following example application where the robot will estimate its foot traction by running head-on into a flat, rigid surface.

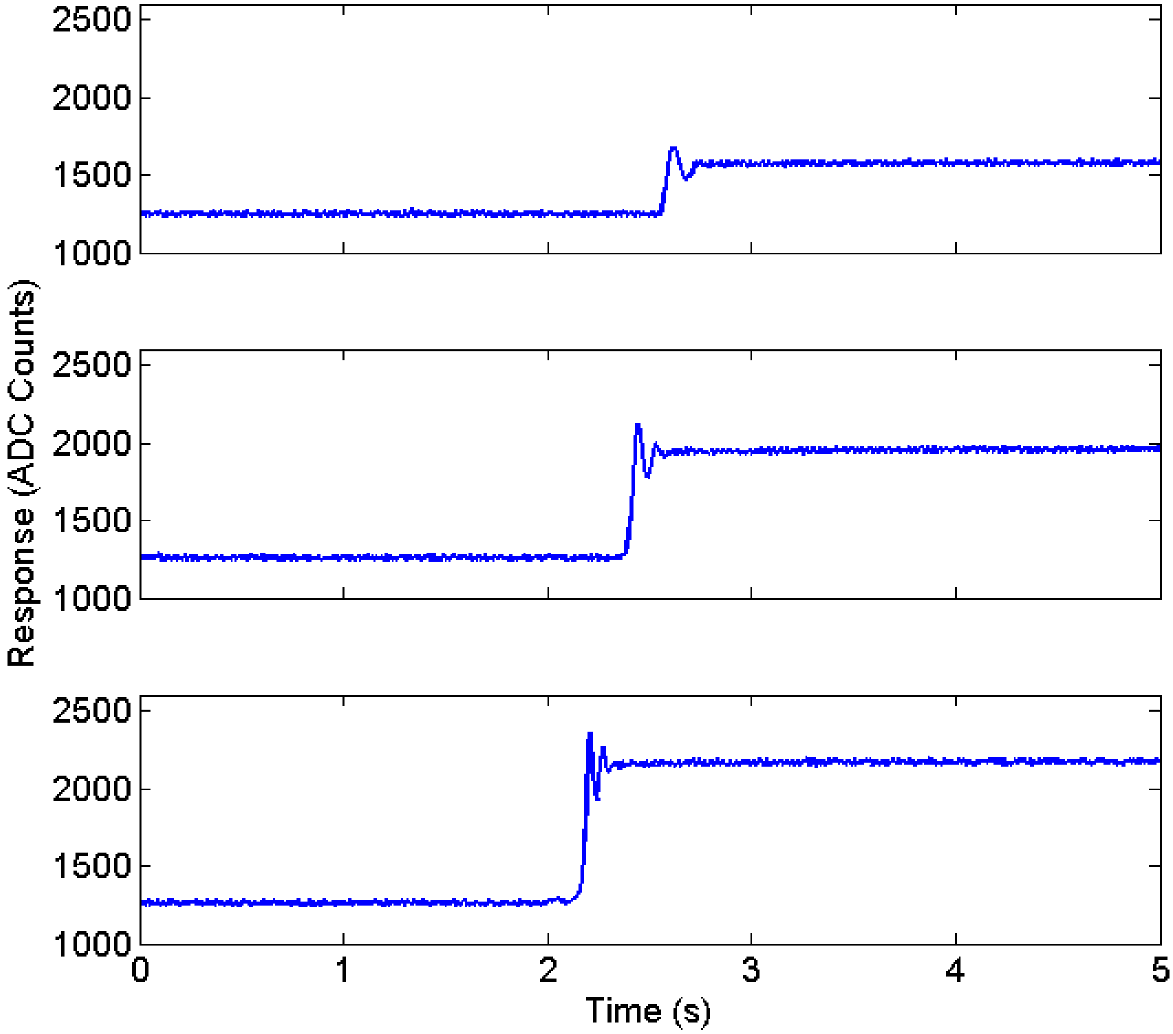

Figure 3.13: Representative positive step responses for a single taxel. Loads were 7.3 gf (top), 14.5 gf (middle), and 25.2 gf (bottom).

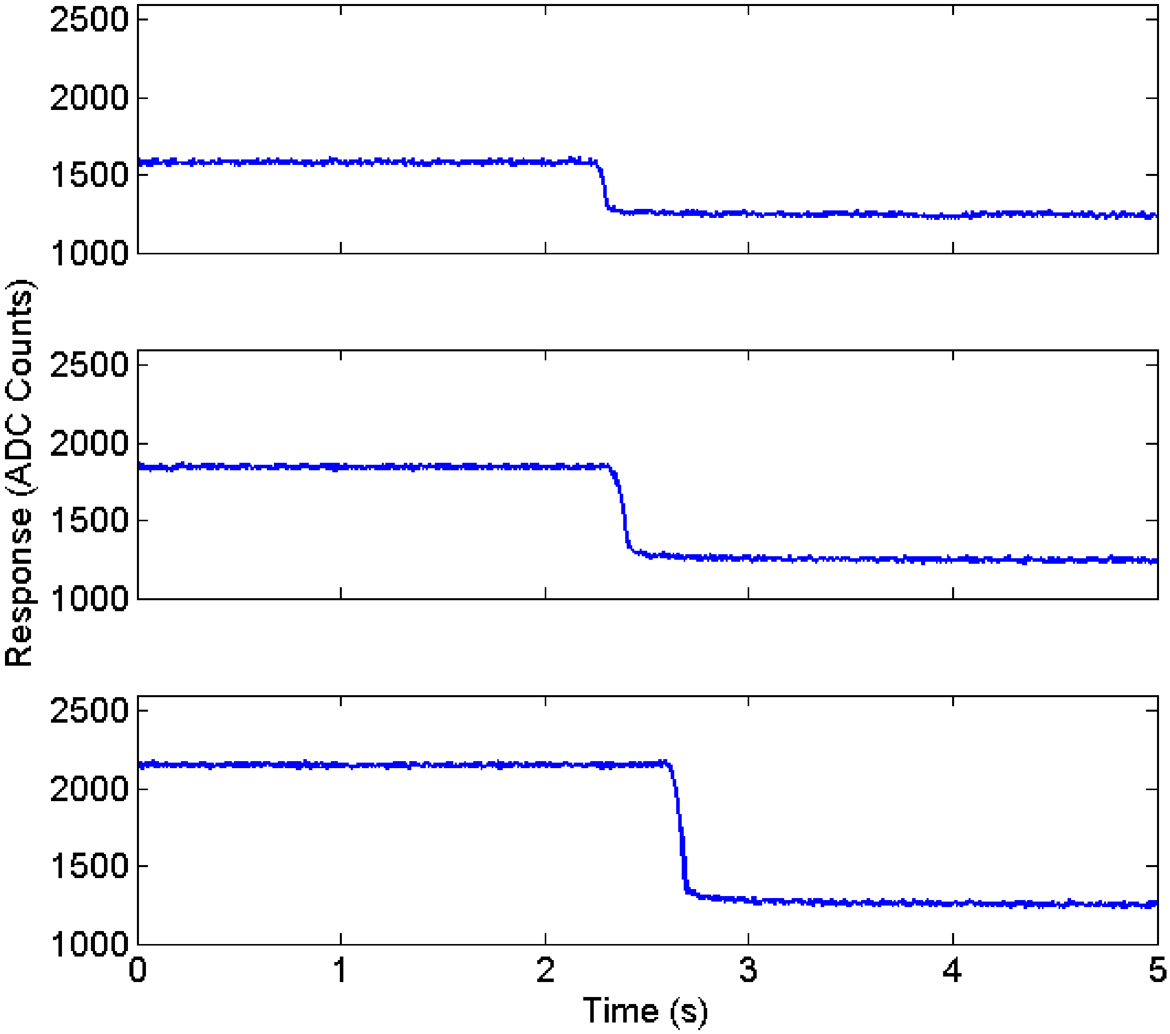

Figure 3.14: Representative negative step responses for a single taxel. Loads were 7.3 gf (top), 14.5 gf (middle), and 25.2 gf (bottom).

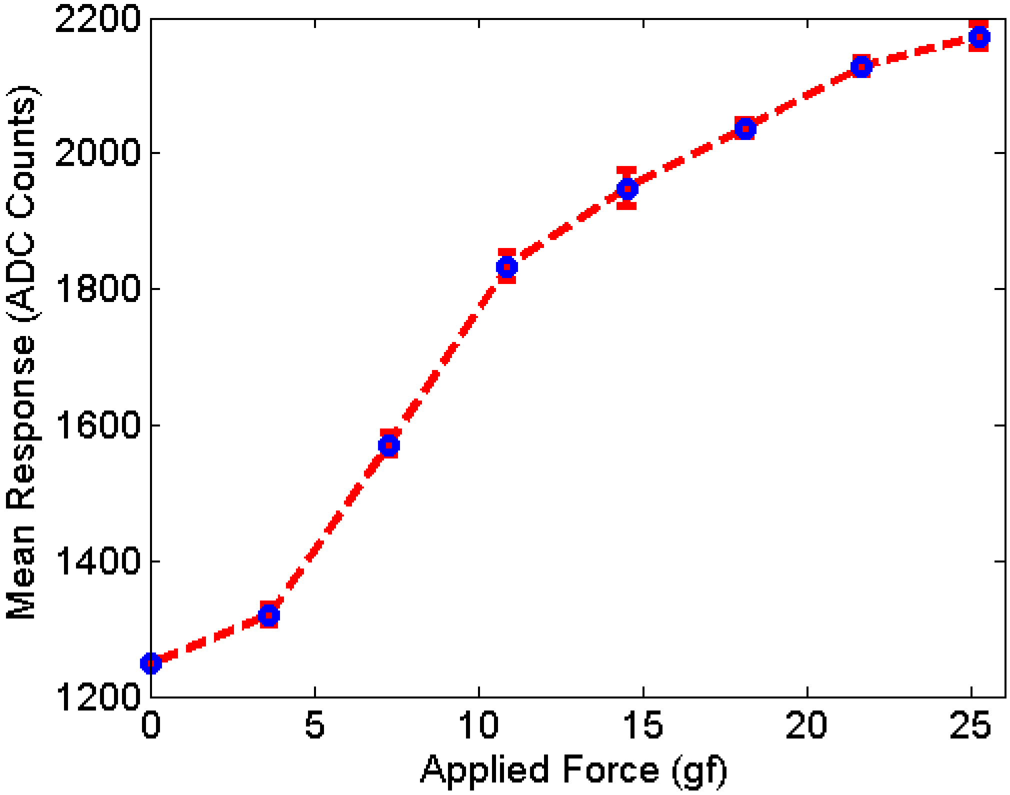

Figure 3.15: Force sensitivity plot for a single taxel. Each blue data point represents the average steady-state response observed over five positive step response trials. Error bars represent ± one standard deviation of the mean steady-state levels from each set of trials.

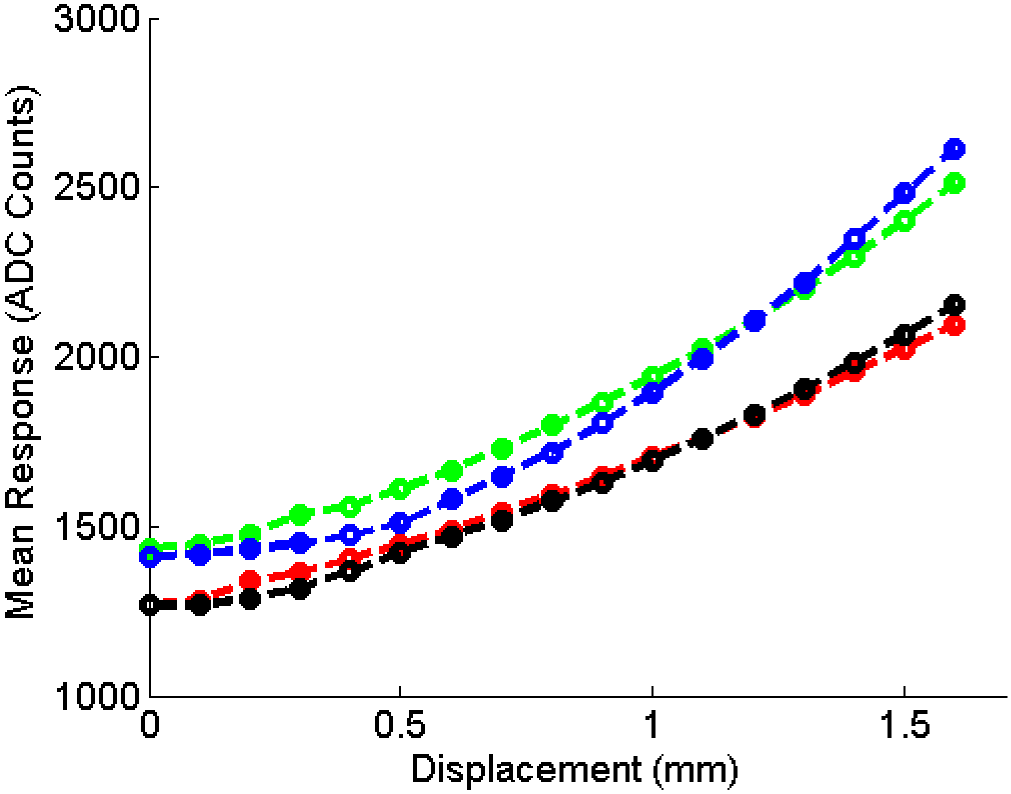

Figure 3.16: Displacement sensitivity plots for four sample taxels. Taxel used for force sensitivity data in Figs. 3.13, 3.14, and 3.15 is shown in black.

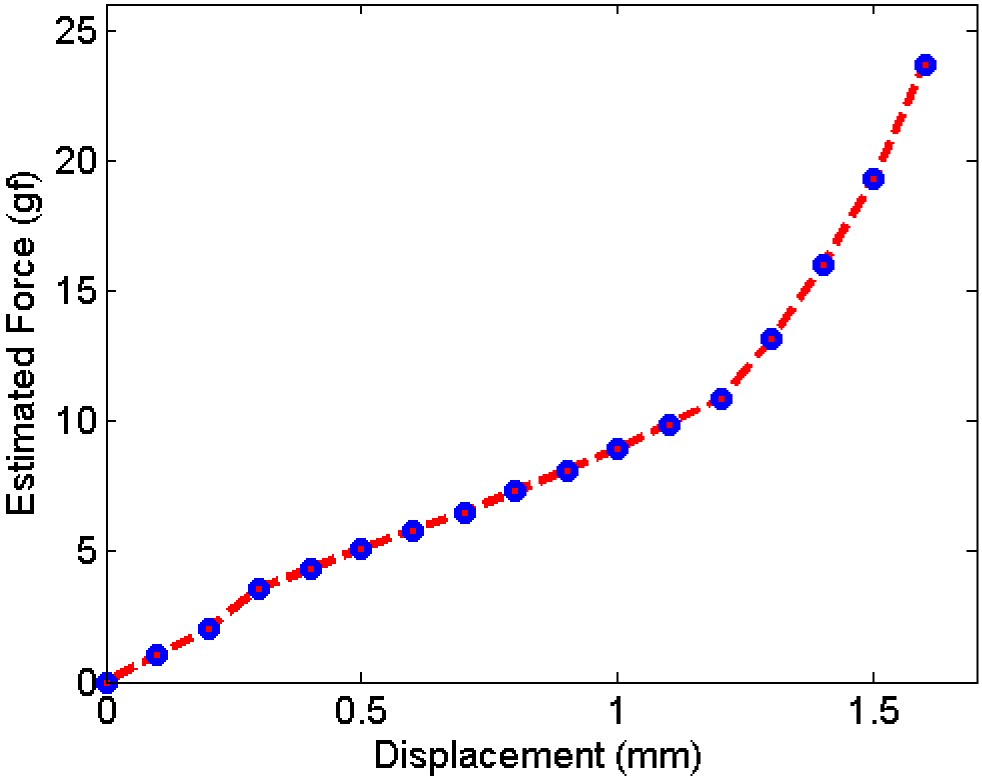

Figure 3.17: Estimated force versus displacement for single taxel. Plot was constructed using Figs. 3.15 and 3.16 to estimate the force needed to achieve each of the experimental displacements.

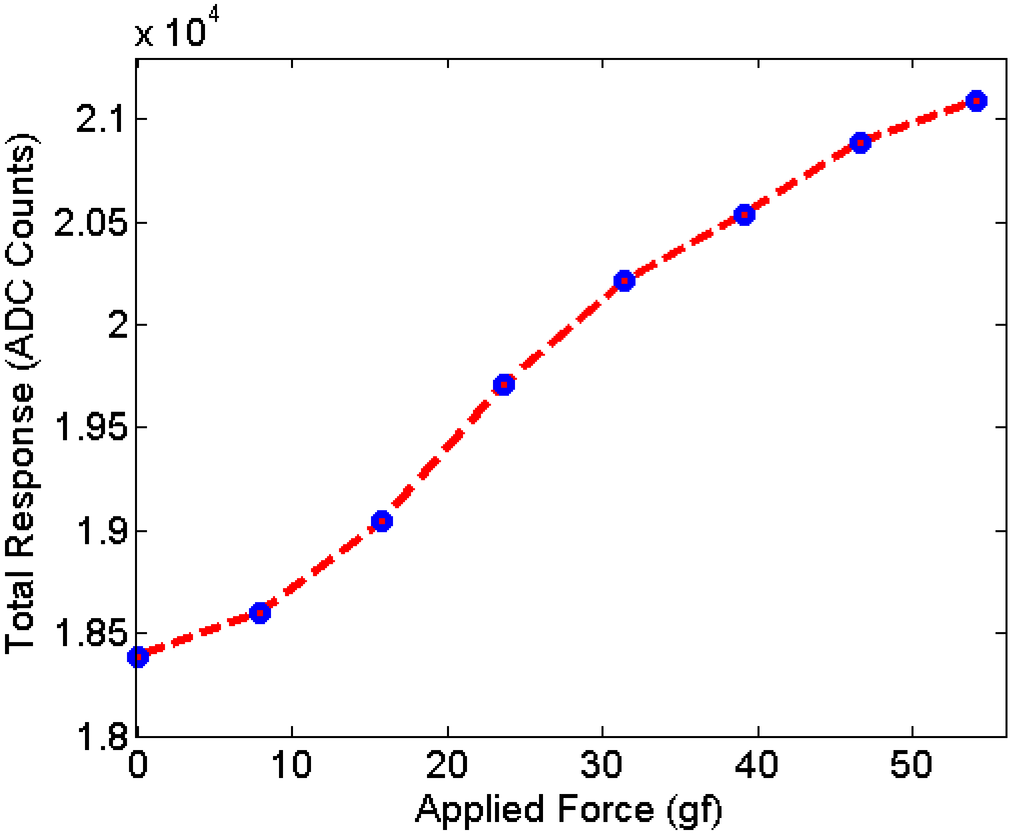

Figure 3.18: Force sensitivity plot for entire bumper pressed against flat, rigid surface. Each blue data point represents the total (sum) steady-state ADC response of the bumper taxels, averaged over five positive step response trials.

3.4 Application: Estimating Foot Traction in New Terrains

The force measurement capability provided by the tactile bumper array enables a number of useful applications in palm-size crawling robots. One application, which is explored here, is to use the force-sensing bumper to estimate the crawler's foot traction in new, unknown environments. Foot traction is an important environmental property for legged robots since it greatly affects locomotion, and is useful knowledge for control, planning, and other tasks. The ability to estimate foot traction upon encountering new terrains is therefore highly-relevant to this domain.

The method used here to estimate foot traction is to have a bumper-equipped robot slowly push itself against a known rigid obstacle, on the unknown terrain, and measure the force build-up until leg slip occurs. The force at which the legs slip serves as an estimate of the maximum force that the robot can generate quasi-statically, and serves as a measure of the foot traction on the unknown terrain. This is inherently an active perception task (Bajcsy 1988 [1]), as the robot is actively modifying the state of the sensor (by pushing it harder against the rigid obstacle) to determine the limit of its available traction.

Foot traction is, in general, a function of numerous parameters including surface and leg geometries, leg contact, material friction properties, surface compliance and so forth. As a simplification, this work focuses on estimating foot traction on largely-uniform rigid surfaces, where the dominant factor in determining foot traction is the coefficient of static friction between the feet and the surface.

Experimental Setup

Three experimental surfaces where tested: vinyl tile, Teflon, and plywood. To estimate the coefficients of friction for these surfaces, a force-sensing bumper array was attached to the front of a variant of the hexapedal VelociRoACH crawler (Fig. 3.1). A large plastic block was taped down to serve as a rigid obstacle, and the robot positioned just in front of it. All trials were carried out in a predetermined starting leg stance, with the four corner legs perpendicular to the ground.

From the starting stance in front of the rigid obstacle, the robot was commanded to move toward the obstacle. The forward thrust was slowly increased by manually increasing the reference level on the motor controller from a computer via wireless link. This process was started at a low level and continued until leg slip was observed visually. A sequence of stills from a trial on the vinyl tile is given in Figure 3.19. Bumper data was collected at 100 Hz (100 bumper frames per second) and stored to an on-board memory during the trials. Data was downloaded from the robot following each trial for offline processing.

To establish a basis for comparison, the static coefficients of friction were also measured through manual experiments. These will be referred to as the empirical friction measurements, to distinguish them from the bumper-based estimates. This was done by fixing the crawler's legs in the same predetermined stance and then attaching a hanging weight (directed over a simple pulley wheel) to the back of the stationary robot. The weight at which the feet slipped was then used to calculate the coefficient of static friction.

Estimation Results and Discussion

A plot of the total bumper activation from the trial shown in Figure 3.19 is given in Figure 3.20. The raw total activation (sum of activation of all taxels) over time is given in blue. The raw total activation is low-pass filtered using a ten-tap trailing window average, the result of which is given in red. As can be seen from the activation curves, the total bumper response increases in distinct bursts as the crawler pushes itself harder against the rigid block, and then drops rapidly at the end of the trial as the feet slip.

The low-passed total activation curves for each trial were converted into force estimates using a whole-bumper force calibration of the bumper array. Representative estimated force curves are given for tile, Teflon, and plywood trials in Figures 3.21, 3.22, and 3.23 respectively. As expected, the robot generates the least traction on Teflon, greater traction on the tile, and the most traction on the plywood surface. An estimate of the static coefficient of friction was extracted from each trial by taking the peak estimated force, assumed to be the point at which the friction barrier was broken, and dividing it by the mass of the robot (46.0 grams).[1]

---

[1] The force was divided by mass, not weight, since the force calibration and force estimate are in units of gram-force (gf).

The empirically-measured static coefficients of friction are plotted in Table 3.1 and the bumper-estimated coefficients in Table 3.2. As can be seen from the data, the friction values for the tile and plywood surfaces exhibit some variance across the trials, both in the empirical measurements as well as the bumper estimates. These surfaces have non-uniform surface textures that result in slightly different foot engagement across trials. The Teflon, which has a uniform surface, does not show as much variation. Overall, the bumper-estimated coefficients match up well with the empirical measurements, achieving a very similar mean and standard deviation on tile and plywood. The bumper estimate for Teflon is slightly higher than what was measured empirically, but still identifies the Teflon as providing significantly less traction than the tile and plywood surfaces.

While these results are preliminary, they demonstrate the feasibility of using the force-sensing tactile bumper to measure leg traction in new environments. Only rigid, near-uniform surfaces were tested here, but the estimation approach is generally applicable to any situation where the robot can push against a rigid obstacle. More data should be collected to better determine the accuracy of this method over different terrains. Future work might also investigate estimating the foot traction as a function of the robot's stance, which will likely influence its traction in most terrains.

Table 3.1: Empirical Friction Measurements

	Trials			**Mean**
Tile	0.31	0.34	0.47	**0.37**
Teflon	0.15	0.17	0.16	**0.17**
Plywood	0.56	0.67	0.72	**0.65**

Table 3.2: Bumper Friction Estimation Results

	Trials			**Mean**
Tile	0.49	0.25	0.42	**0.39**
Teflon	0.25	0.31	0.18	**0.25**
Plywood	0.63	0.57	0.71	**0.64**

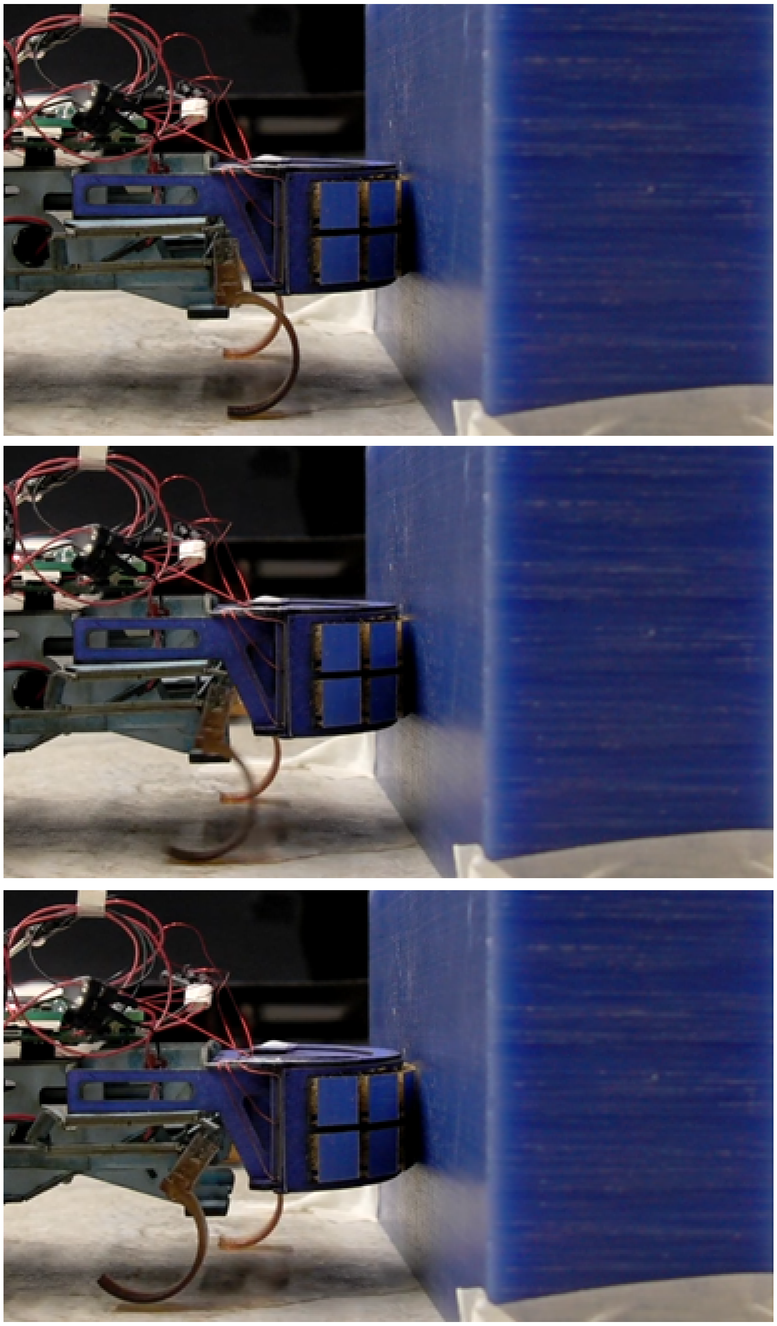

Figure 3.19: Sequence of stills from an example friction estimation trial. The hexapedal crawler pushes against a rigid surface with gradually increasing thrust until leg slip occurs.

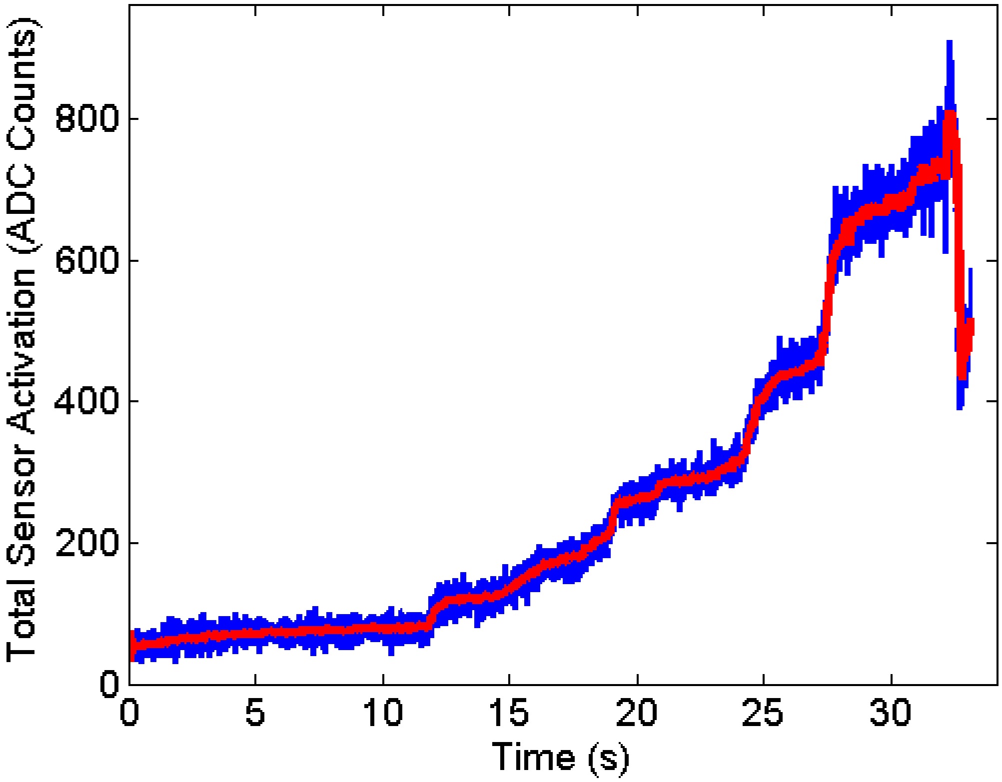

Figure 3.20: Plot of tactile bumper response during friction estimation trial shown in Fig. 3.19. Blue curve represents raw total response, while red curve represents low-pass filtered response.

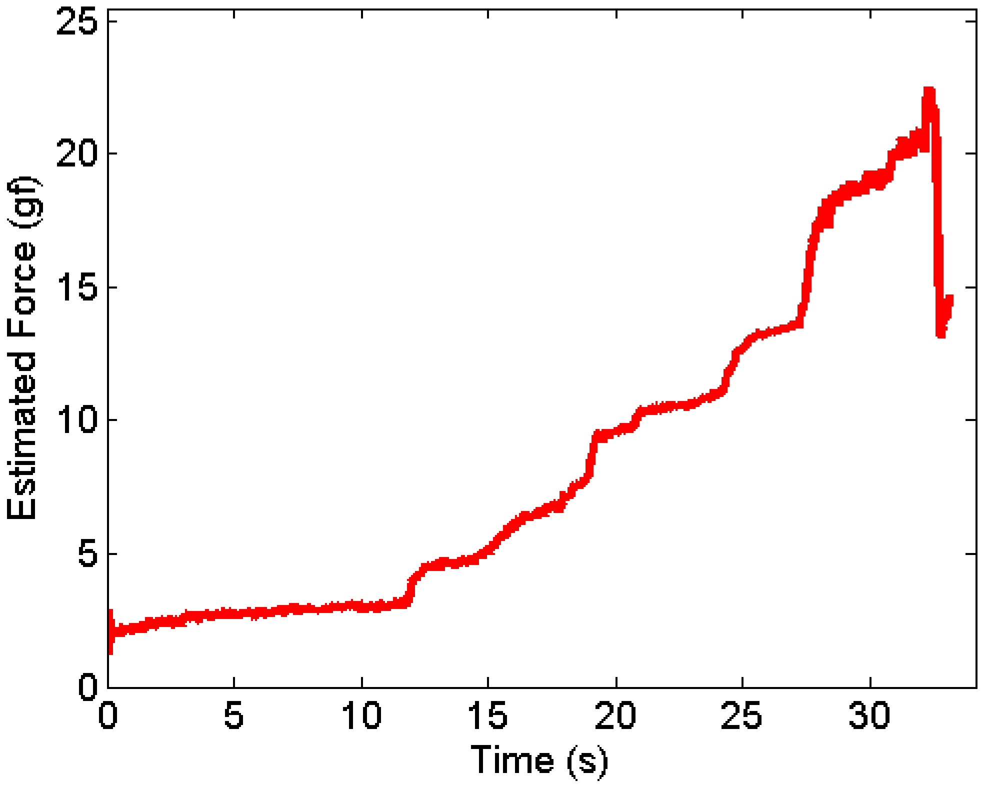

Figure 3.21: Plot of estimated force exerted by tactile bumper during friction estimation trial on vinyl tile surface shown in Fig. 3.19.

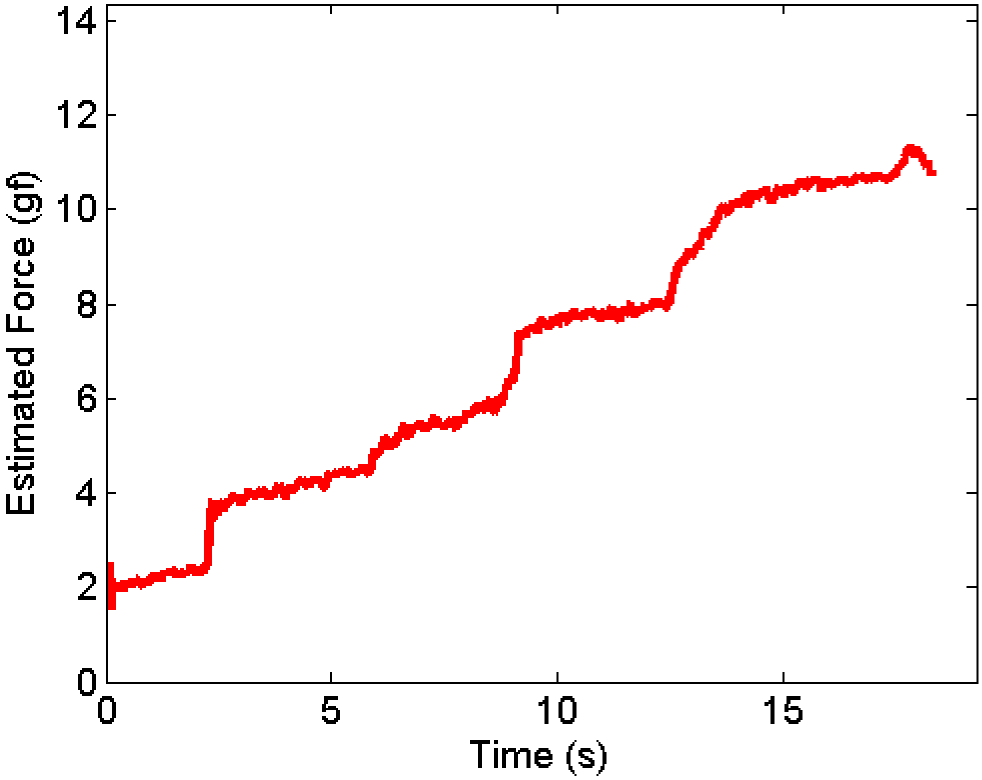

Figure 3.22: Plot of estimated force exerted by tactile bumper during friction estimation trial on Teflon surface.

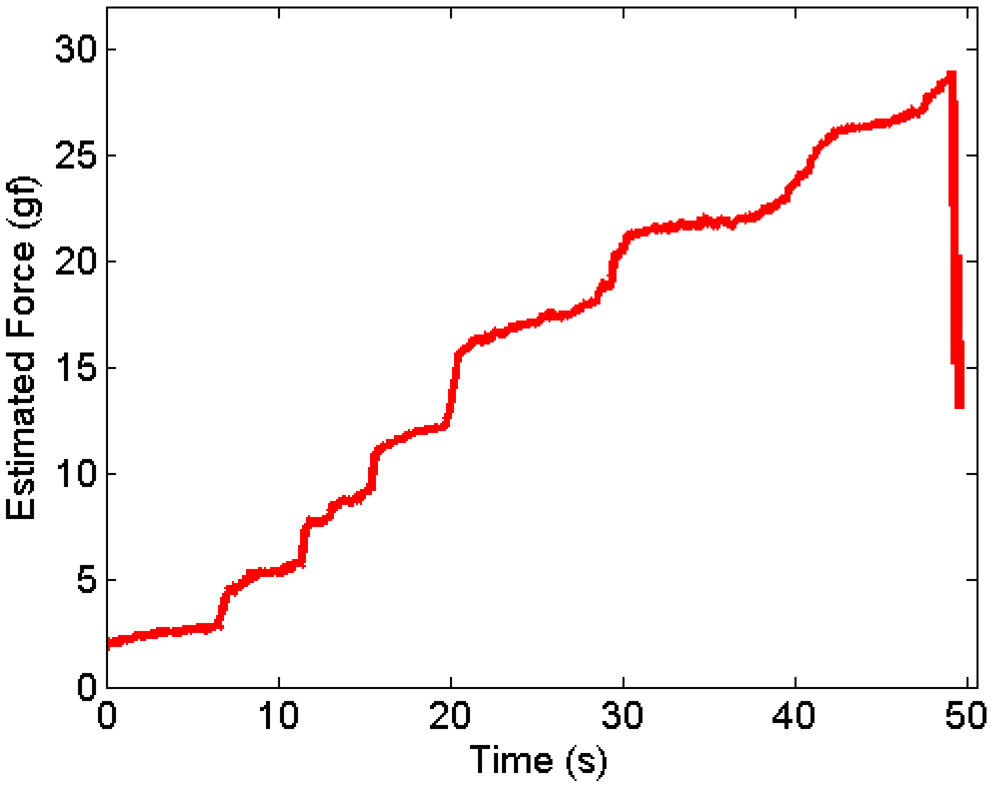

Figure 3.23: Plot of estimated force exerted by tactile bumper during friction estimation trial on plywood surface.

Chapter 4

Conclusion

Two novel, low-cost tactile sensors for palm-size crawling robots have been presented in this work. The first of these, the binary hair sensor array, combines a bio-inspired sensing mechanism with a convenient laminar design resulting in a rapidly-manufacturable sensor with sufficient sensitivity to detect contact forces under one gram-force (10 mN). The polymer hairs provide a versatile sensing modality as they readily detect both normal and shear forces. In a sample application with a hexapedal crawler, it was shown that the hair sensor array could be used to estimate average ground speed and to detect high-centering when running over simple obstacles by tracking the propagation of contact along the base of the robot. Future work might investigate using a higher resolution analog hair array to perform similar estimation tasks in more complex, natural environments.

In order to collect more detailed tactile data than was available from the binary sensor, a second tactile sensor was designed. The second sensor, an analog tactile bumper array, provides crawling robots with the ability to measure contact forces experienced when colliding with obstacles. The sensor design is both cheap and easy to fabricate, and has adequate sensitivity and bandwidth for measuring a robot's interactions with environmental obstacles. As an example application, the force-sensing tactile bumper was used to estimate a hexapedal robot's traction in different terrains, by measuring the contact forces produced when pushing against a rigid obstacle. The estimated coefficients of these trials closely matched empirically-measured coefficients for the experimental surfaces, suggesting that the bumper-based traction estimation method could be a a reliable way to measure a robot's traction in new, unknown surfaces. The method generalizes to any environment in which a rigid obstacle can be found, and future work could collect more data, over a larger variety of terrains to determine the extent to which the method can be applied.

Acknowledgments

I would like to thank my advisor, Professor Ron Fearing, for his insights, advice and support throughout the course of this work, as well as my peers in the Biomimetic Millisystems Lab for all their help and suggestions. I would also like to thank Professor Ruzena Bajcsy for serving as the second reader for this report, and more generally for everything that I have learned from her courses. Many thanks to Duncan Haldane for providing his crawling robot designs for use in my experiments and also for his robot design description, included in Chapter 2. Additionally, I would like to thank Professor Will Provancher (Univ. of Utah) for his advice while visiting our group on sabbatical. This work has been supported by the DARPA Maximum Mobility and Manipulation (M3) program.

Appendix A

Binary SkinProc Schematic

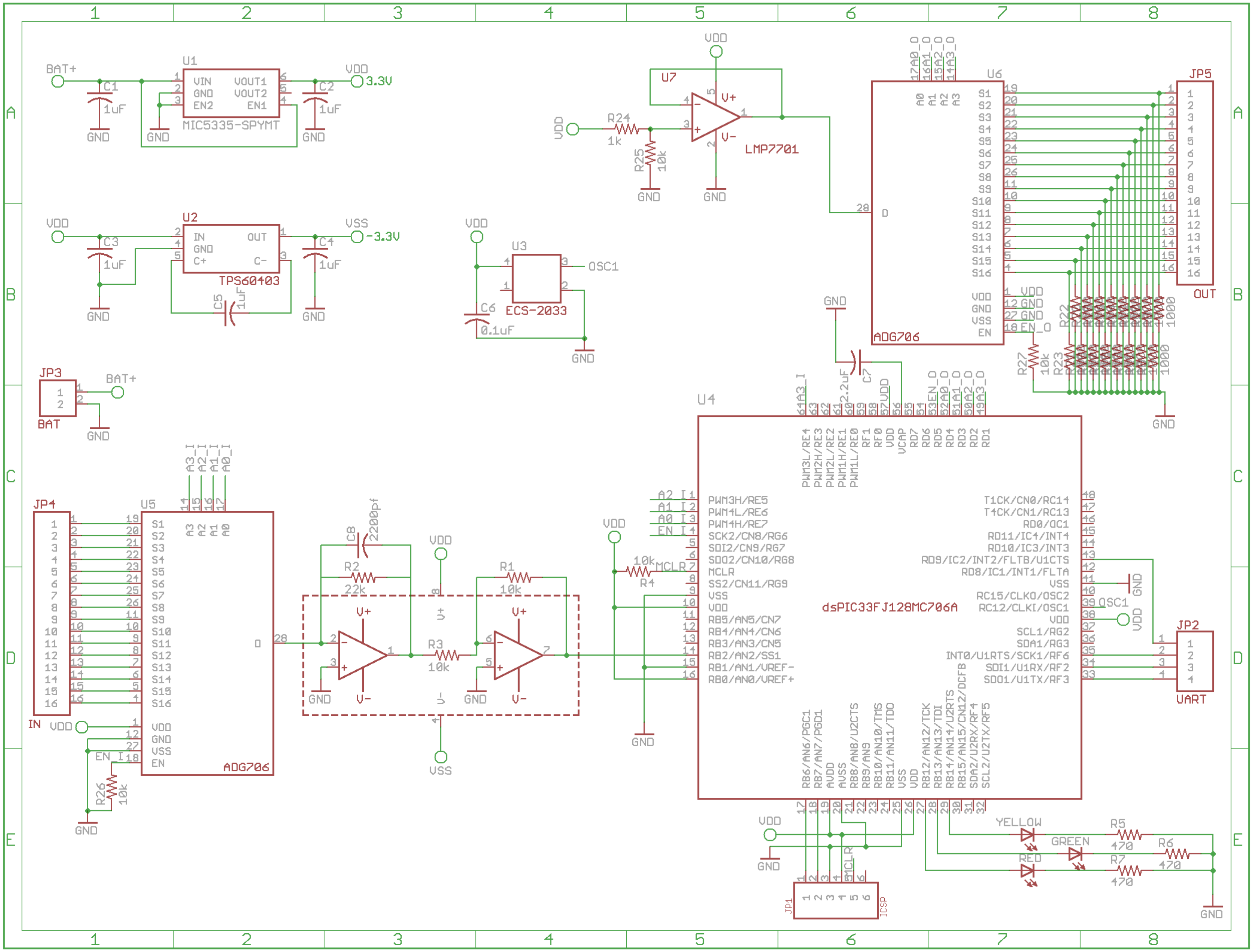
BAT+
C1
1uF
U1
VIN
GND
EN2
VOUT1
VOUT2
EN1
MIC5335-SPYMT
VDD
3.3V
C2
1uF
GND
VDD
C3
1uF
U2
IN
GND
C+
OUT
C-
TPS60403
C5
1uF
VSS
-3.3V
C4
1uF
JP3
BAT
U3
OSC1
ECS-2033
C6
0.1uF
U7
V+
V-
LMP7701
R24
1k
R25
10k
U6
A0
A1
A2
A3
17A0_O
16A1_O
15A2_O
14A3_O
S1
S2
S3
S4
S5
S6
S7
S8
S9
S10
S11
S12
S13
S14
S15
S16
D
VDD
GND
VSS
EN
EN_O
ADG706
JP5
OUT
R22
1000
R23
R27
10k
C7
2.2uF
U4
dsPIC33FJ128MC706A
PWM3L/RE4
PWM2H/RE3
PWM2L/RE2
PWM1H/RE1
PWM1L/RE0
RF1
RF0
VDD
VCAP
RD7
RD6
RD5
RD4
RD3
RD2
RD1
PWM3H/RE5
PWM4L/RE6
PWM4H/RE7
SCK2/CN8/RG6
SDI2/CN9/RG7
SDO2/CN10/RG8
MCLR
SS2/CN11/RG9
VSS
VDD
RB5/AN5/CN7
RB4/AN4/CN6
RB3/AN3/CN5
RB2/AN2/SS1
RB1/AN1/VREF-
RB0/AN0/VREF+
T1CK/CN0/RC14
T4CK/CN1/RC13
RD0/OC1
RD11/IC4/INT4
RD10/IC3/INT3
RD9/IC2/INT2/FLTB/U1CTS
RD8/IC1/INT1/FLTA
VSS
RC15/CLKO/OSC2
RC12/CLKI/OSC1
VDD
SCL1/RG2
SDA1/RG3
INT0/U1RTS/SCK1/RF6
SDI1/U1RX/RF2
SDO1/U1TX/RF3
RB6/AN6/PGC1
RB7/AN7/PGD1
AVDD
AVSS
RB8/AN8/U2CTS
RB9/AN9
RB10/AN10/TMS
RB11/AN11/TDO
VSS
VDD
RB12/AN12/TCK
RB13/AN13/TDI
RB14/AN14/U2RTS
RB15/AN15/CN12/OCFB
SDA2/U2RX/RF4
SCL2/U2TX/RF5
R4
10k
JP2
UART
YELLOW
GREEN
RED
R5
470
R6
470
R7
470
JP1
ICSP
MCLR
JP4
IN
U5
ADG706
A3_I
A2_I
A1_I
A0_I
EN_I
R26
10k
C8
2200pf
R2
22k
R3
10k
R1
10k
V+
V-
VSS
1
2
3
4
5
6
7
8
A
B
C
D
E

Appendix B

Analog SkinProc Schematic

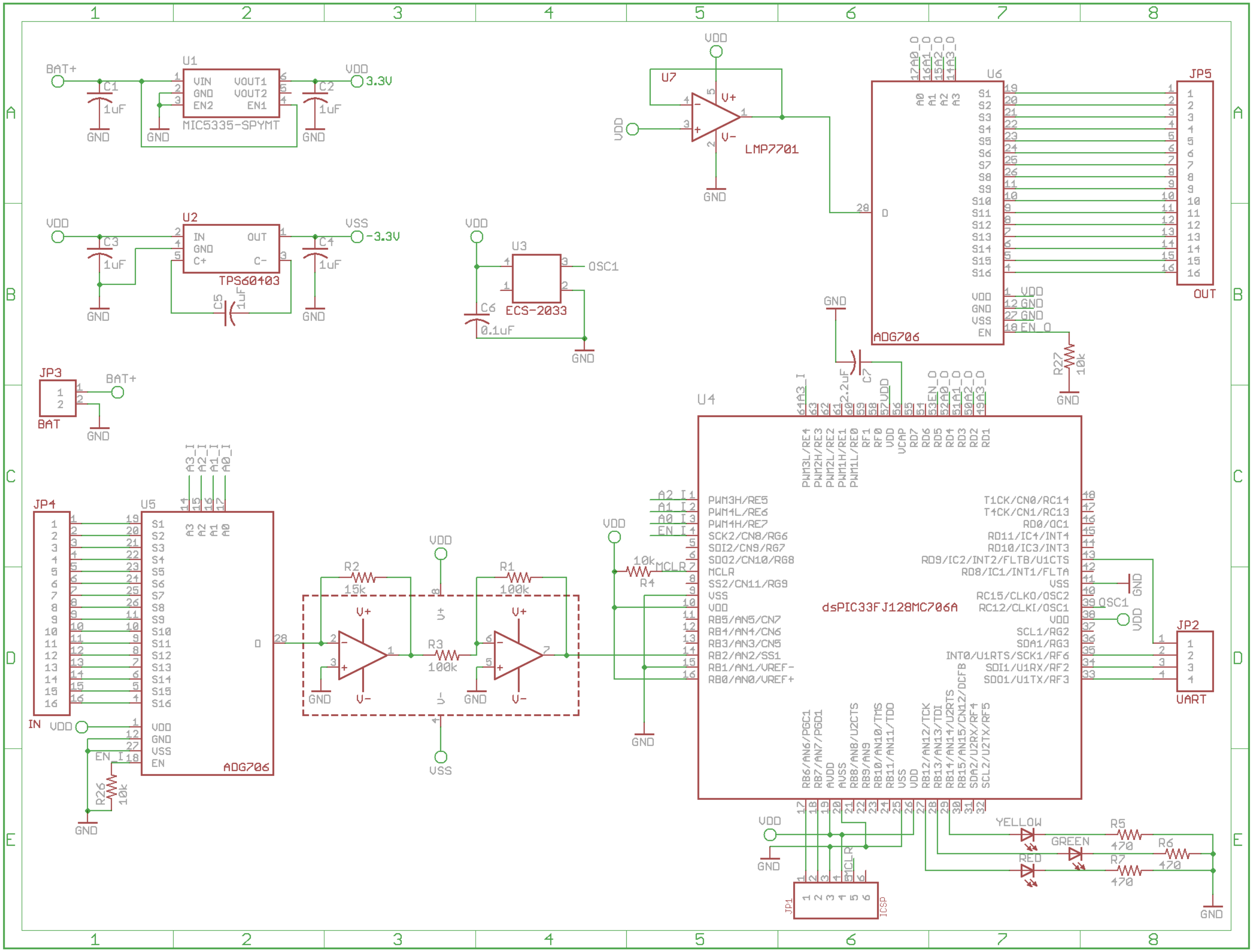
BAT+
C1
1uF
GND
U1
VIN
GND
EN2
VOUT1
VOUT2
EN1
MIC5335-SPYMT
C2
VDD
3.3V
U2
IN
OUT
C+
C-
TPS60403
C3
C4
C5
VSS
-3.3V
U3
ECS-2033
OSC1
C6
0.1uF
U7
V+
V-
LMP7701
U6
ADG706
S1
S2
S3
S4
S5
S6
S7
S8
S9
S10
S11
S12
S13
S14
S15
S16
D
A0
A1
A2
A3
EN
EN_O
JP5
OUT
R27
10k
C7
2.2uF
JP3
BAT
U4
dsPIC33FJ128MC706A
MCLR
R4
10k
JP2
UART
JP4
IN
U5
EN_I
R26
R2
15k
R1
100k
R3
100k
JP1
ICSP
YELLOW
GREEN
RED
R5
R6
R7
470

Appendix C

Flex-Circuit Schematic

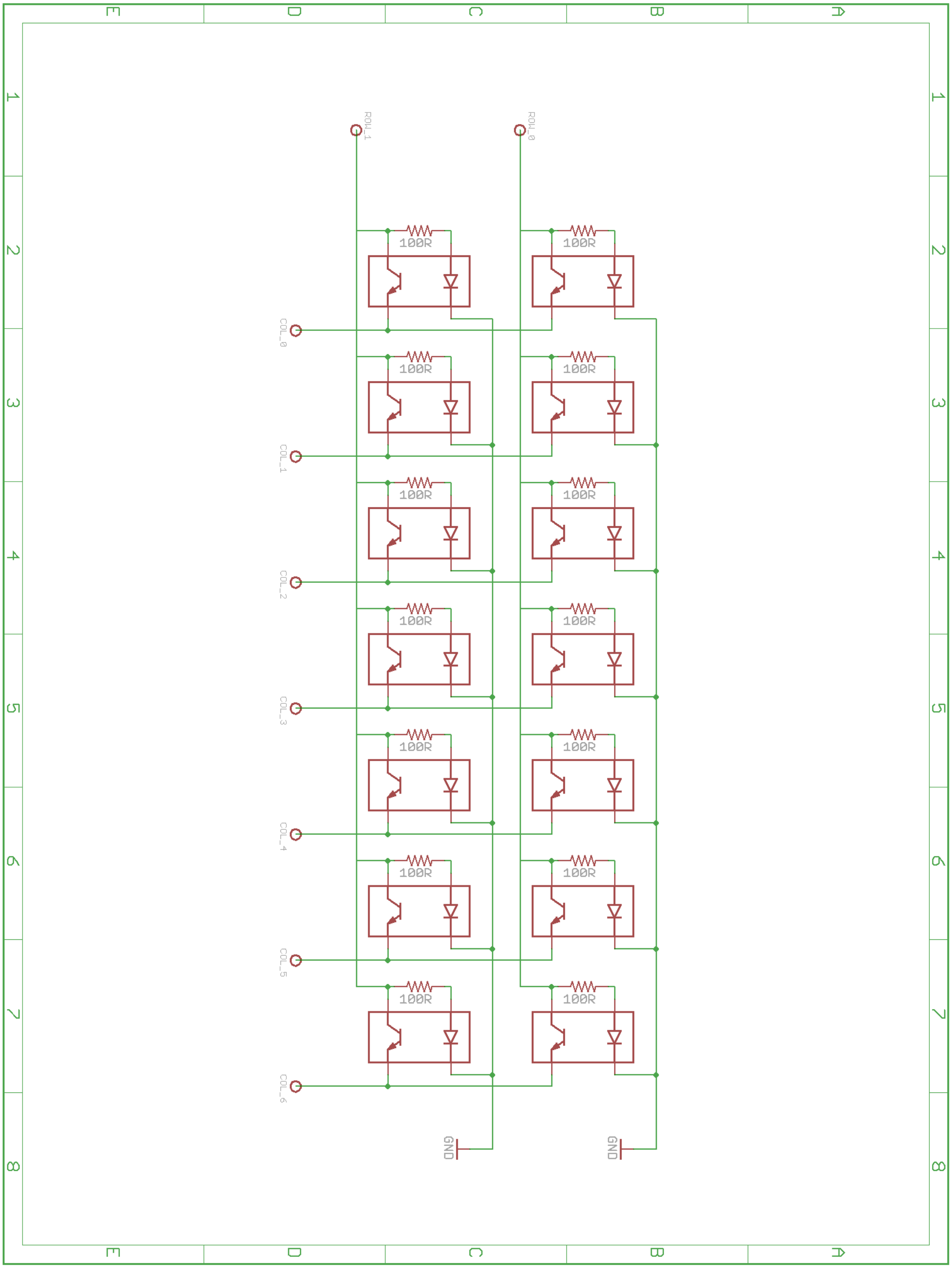
E
D
C
B
A
1
2
3
4
5
6
7
8
ROW_1
ROW_0
COL_0
COL_1
COL_2
COL_3
COL_4
COL_5
COL_6
100R
GND

Bibliography

[1] R. Bajcsy. “Active perception”. In: *Proceedings of the IEEE* 76.8 (1988), pp. 966–1005. ISSN: 0018-9219. DOI: `10.1109/5.5968`.

[2] P. Birkmeyer, K. Peterson, and R.S. Fearing. “DASH: A dynamic 16g hexapedal robot”. In: *IEEE/RSJ Int. Conf. on Intelligent Robots and Systems.* 2009, pp. 2683 –2689. DOI: `10.1109/IROS.2009.5354561`.

[3] N.J. Cowan, E.J. Ma, M. Cutkosky, and R.J. Full. “A Biologically Inspired Passive Antenna for Steering Control of a Running Robot”. In: *Robotics Research.* Ed. by Paolo Dario and Raja Chatila. Vol. 15. Springer Tracts in Advanced Robotics. Springer Berlin / Heidelberg, 2005, pp. 541–550. ISBN: 978-3-540-23214-8.

[4] M. Fend. “Whisker-Based Texture Discrimination on a Mobile Robot”. In: *Advances in Artificial Life.* Ed. by Mathieu Capcarrre, Alex Freitas, Peter Bentley, Colin Johnson, and Jon Timmis. Vol. 3630. Lecture Notes in Computer Science. Springer Berlin / Heidelberg, 2005, pp. 302–311. ISBN: 978-3-540-28848-0.

[5] M. Fend, S. Bovet, H. Yokoi, and R. Pfeifer. “An active artificial whisker array for texture discrimination”. In: *IEEE/RSJ Int. Conf. on Intelligent Robots and Systems.* Vol. 2. 2003, 1044 –1049 vol.2. DOI: `10.1109/IROS.2003.1248782`.

[6] C. Fox, B. Mitchinson, M. Pearson, A. Pipe, and T. Prescott. “Contact type dependency of texture classification in a whiskered mobile robot”. In: *Autonomous Robots* 26 (4 2009), pp. 223–239. ISSN: 0929-5593.

[7] D.W. Haldane, K.C. Peterson, F.L. Garcia Bermudez, and R.S. Fearing. “Animal-Inspired Design and Aerodynamic Stabilization of a Hexapedal Millirobot”. In: *IEEE Int. Conf. on Robotics and Automation.* 2013.

[8] S. Hirose, S. Inoue, and K. Yoneda. “The whisker sensor and the transmission of multiple sensor signals”. In: *Advanced Robotics* 4.2 (1990), pp. 105 –117.

[9] A.M. Hoover and R.S. Fearing. “Fast scale prototyping for folded millirobots”. In: *IEEE Int. Conf. on Robotics and Automation*. 2008, pp. 886 –892. DOI: `10.1109/ROBOT.2008.4543317`.

[10] A.M. Hoover, S. Burden, Xiao-Yu Fu, S.S. Sastry, and R.S. Fearing. “Bio-inspired design and dynamic maneuverability of a minimally actuated six-legged robot”. In: *IEEE RAS and EMBS Int. Conf. on Biomedical Robotics and Biomechatronics*. 2010, pp. 869 –876. DOI: `10.1109/BIOROB.2010.5626034`.

[11] J.Y. Jun, D. Haldane, and J.E. Clark. “Compliant Leg Shape, Reduced-Order Models and Dynamic Running”. In: *International Symposium on Experimental Robotics*. 2010, pp. 1–15.

[12] D. Jung and A. Zelinsky. “Whisker based mobile robot navigation”. In: *IEEE/RSJ Int. Conf. on Intelligent Robots and Systems*. Vol. 2. 1996, 497 –504 vol.2. DOI: `10.1109/IROS.1996.570842`.

[13] A.G. Lamperski, O.Y. Loh, B.L. Kutscher, and N.J. Cowan. “Dynamical Wall Following for a Wheeled Robot Using a Passive Tactile Sensor”. In: *IEEE Int. Conf. on Robotics and Automation*. 2005, pp. 3838 –3843. DOI: `10.1109/ROBOT.2005.1570706`.

[14] J Lee, S.N. Sponberg, O.Y. Loh, A.G. Lamperski, R.J. Full, and N.J. Cowan. “Templates and Anchors for Antenna-Based Wall Following in Cockroaches and Robots”. In: *Robotics, IEEE Transactions on* 24.1 (2008), pp. 130 –143. ISSN: 1552-3098. DOI: `10.1109/TRO.2007.913981`.

[15] N.F. Lepora, M. Evans, C.W. Fox, M.E. Diamond, K. Gurney, and T.J. Prescott. “Naive Bayes texture classification applied to whisker data from a moving robot”. In: *Int. Joint Conf. on Neural Networks (IJCNN)*. 2010, pp. 1 –8. DOI: `10.1109/IJCNN.2010.5596360`.

[16] A.O. Pullin, N.J. Kohut, and D. Zarrouk. “Dynamic turning of 13 cm robot comparing tail and differential drive”. In: *IEEE Int. Conf. on Robotics and Automation*. 2012.

[17] R.A. Russell and J.A. Wijaya. “Object location and recognition using whisker sensors”. In: *Australasian Conf. on Robotics and Automation*. 2003.

[18] R.A. Russell and J.A. Wijaya. “Recognising and manipulating objects using data from a whisker sensor array”. In: *Robotica* 23.05 (2005), pp. 653–664. DOI: `10.1017/S0263574704000748`. eprint: `http://journals.cambridge.org/article_S0263574704000748`. URL: `http://dx.doi.org/10.1017/S0263574704000748`.

[19] A.E. Schultz, J.H. Solomon, M.A. Peshkin, and M.J. Hartmann. “Multifunctional Whisker Arrays for Distance Detection, Terrain Mapping, and Object Feature Extraction”. In: *IEEE Int. Conf. on Robotics and Automation*. 2005, pp. 2588 –2593. DOI: `10.1109/ROBOT.2005.1570503`.

[20] A.K. Seth, J.L. McKinstry, G.M. Edelman, and J.L. Krichmar. “Texture discrimination by an autonomous mobile brain-based device with whiskers”. In: *IEEE Int. Conf. on Robotics and Automation*. Vol. 5. 2004, 4925 –4930 Vol.5. DOI: `10.1109/ROBOT.2004.1302498`.

[21] J.A. Wijaya and R.A. Russell. “Object exploration using whisker sensors”. In: *Australasian Conf. on Robotics and Automation*. 2002, pp. 180–185.